

Analysis of the plasma response in a 5kW class HET from a 2Dzr PIC model

A. Marín-Cebrián,¹ E. Ahedo,¹ and A. Domínguez-Vázquez²

¹⁾Department of Aerospace Engineering, Universidad Carlos III de Madrid, Leganés, Spain

²⁾Department of Fluid Mechanics, Universidad de Málaga, Málaga, Spain

(*Electronic mail: almarinc@pa.uc3m.es)

(Dated: 21 May 2025)

AM: TBD

A two-dimensional particle-in-cell model has been applied to simulate axial-radial plasma response in a virtual 5kW Hall thruster which resembles the PPS@5000. The time evolution of plasma currents to the domain boundaries shows convergence and the time-averaged steady-state solution is analyzed. The plasma response is strongly affected by the complex magnetic field topology. The curved magnetic field near the anode effectively inhibits the radial plasma motion, reducing particle and energy losses to the walls. The simulation results suggest that the Debye sheaths at the lateral dielectric walls may collapse for a grazing magnetic field incidence angle. The analysis of the radial electron momentum equation reveals a balance between the pressure gradient, electric and magnetic forces. The dominant terms in such equation change depending on the magnetic field curvature. Near the exit, the magnetic field is almost radial and the pressure gradient and electric force approximately balance each other. Near the anode, the magnetic field is curved towards the anode and the dominant terms in the equation are the pressure and magnetic forces. The radial magnetic force depends on the azimuthal electron current, which is found to be a combination of $E \times B$ and diamagnetic drifts. The azimuthal momentum balance, which determines the axial electron current, reveals that Finite-Larmor-Radius effects become important near the anode.

I. INTRODUCTION

Currently, a large part of Hall Effect Thruster (HET) numerical research relies on 2D axial-radial (2Dzr) hybrid models^{1,2}, treating heavy species (i.e. ions and neutrals) with a particle-in-cell (PIC) formulation and electrons as a drift-diffusive fluid. EA: esta afirmación tan fuerte necesita de más referencias que 2, o reformular la frase The standard macroscopic formulation for electrons is based on the assumption that their velocity distribution function (VDF) is (near) Maxwellian³. However, the low collisionality in the HET channel prevents the plasma from reaching local thermodynamic equilibrium; and thus, standard fluid models can misrepresent some relevant physics⁴. Alternatively, kinetic models do not make any assumptions on the VDF shape; but the wide range of time and length scales that need to be resolved make multidimensional simulations challenging⁵.

Recently, we have developed the 2D PIC model PICASO^{6,7} to analyze the kinetic response of the HET plasma. In a previous work⁷, we applied this model to simulate the axial-radial plasma dynamics in a simplified HET configuration featuring a perfectly radial magnetic field, in the quasiplanar limit (i.e., cylindrical effects were neglected) and only considering ionization and anomalous collisions for electrons. The analysis focused mainly on the electron response and the kinetic solution revealed important differences with respect to standard fluid models: (1) plasma-wall interaction parameters can differ largely from classical theory, based on a

Maxwellian VDF, (2) the electron heat flux has a complex behavior and, in general, it cannot be described by a Fourier-type law, and (3) the pressure tensor is composed of a gyrotrropic anisotropic part and small gyroviscous terms. Indeed, near the anode, gyroviscosity and inertia are relevant in the azimuthal electron momentum equation, where dominant terms are two orders of magnitude smaller than those in the axial momentum equation.

However, the magnetic field topology in HETs is curved. EA: con diferentes configuraciones en distintos prototipos (lente magnético, a pantalla mágnetico, puntos nulos cerca de ánodo, etc.) Experimental^{8,9} and numerical^{10,11} AM: revisar citas EA: el artículo de miedzik no puede ir aquí? works, have shown that oblique magnetic fields can reduce plasma fluxes to the walls and enhance the thruster performances. EA: alternativa: in ref.¹², a 1D radial (1Dr) PIC model showed, first, a significant reduction in electron anisotropy when the magnetic field is moderately-curved magnetic field and, second, a reduction of the plasma fluxes to the radial walls when la componente magnética radial es confinante. (que añade nuestro trabajo numérico a los anteriores?) In one of our previous works¹², we used a 1D radial (1Dr) PIC model to investigate the effect of a moderately-curved magnetic field in the radial plasma behavior. The kinetic solution showed a significant reduction in electron anisotropy, in agreement with Ref. 13. A magnetic force term, which can be electron confining or expanding, appears in the radial momentum equation and modifies the relative relevance

of the radial pressure gradient and electric force density. As a consequence, the plasma density near the wall and the degree of radial ion defocusing were affected. However, such study was limited by the intrinsic shortcomings of a 1Dr model. A consistent analysis of the impact of the magnetic field topology requires a 2Dzr model of the discharge.

In this work we extend the model of Ref. 7 to afford the simulation of more realistic configurations, including a complex magnetic topology, cylindrical effects and $e-n$ collisions. The simulated scenario takes the inputs of a virtual 5kW Hall thruster which resembles the PPS@5000 **EA: aquí tienes que dar alguna referencia del motor real y quizás citar domi22a** and the analysis focuses on the steady-state plasma response. The effect of the curved magnetic field on the macroscopic plasma response and plasma-wall interaction magnitudes are discussed. The analysis of the electron momentum equation explains some aspects of the macroscopic plasma response and reveals the important terms along the axial, radial and azimuthal directions. **EA: creo que este párrafo le falta algunas cosas para justificar mejor este trabajo**

The article is structured as follows. Section II summarizes the main aspects of the kinetic model. Section III presents and analyzes the simulation results for the proposed scenario. Macroscopic plasma magnitudes, wall interaction parameters and the electron momentum equation satisfied by the kinetic electrons are under scrutiny. Finally, conclusions are gathered in Section VII. Preliminary results of this work were presented at the 38th International Electric Propulsion Conference¹⁴.

II. THE KINETIC MODEL

The axisymmetric (i.e. $\partial/\partial\theta = 0$) 2Dzr PIC model, PICASO, aims to solve the plasma response in a Hall thruster discharge. This Section summarizes the the main features of the kinetic code and the model input parameters are gathered in Table I.

Figure 1 provides a sketch of the simulation domain, comprising the thruster channel and a small portion of the near plume. The domain boundaries are defined by the metallic anode (A), the dielectric thruster walls (W), and the downstream plume boundary, which acts as the cathode/neutralizer (N). The thruster has dimensions $L = 29$ mm, $r_{W1} = 54.5$ mm and $r_{W2} = 76.7$ mm for the length, inner and outer radii of the annular channel respectively. The simulation domain extends up to three channel lengths along the axial direction, and approximately three channel widths along the radial direction in the near-plume region.

Electrons, e , and singly charged xenon ions, i , are simulated as two different populations of macroparticles with constant weight (i.e. number of elementary particles per simulated macroparticle). Explicit time integration of particle trajectories is performed using the Boris

algorithm¹⁵ and cylindrical effects on the particle motion are accounted for as described in Ref. 16. First-order weighting schemes (Cloud-In-Cell) are used for both, interpolating \mathbf{B} and \mathbf{E} to the particle position, and calculating integral moments of each species VDF (i.e. the macroscopic magnitudes) at the mesh nodes. The main macroscopic magnitudes of interest for species s are the density n_s , the particle flux vector $n_s \mathbf{u}_s$, the momentum flux tensor $\bar{\mathbf{M}}_s$, and the energy flux vector \mathbf{P}_s'' , defined, respectively, as

$$n_s = \iiint f_s d^3v, \quad n_s \mathbf{u}_s = \iiint v f_s d^3v, \\ \bar{\mathbf{M}}_s = m_s \iiint v \mathbf{v} f_s d^3v, \quad \mathbf{P}_s'' = \frac{m_s}{2} \iiint v v^2 f_s d^3v. \quad (1)$$

Electron and ion particles reaching any of the domain boundaries contribute to the electric current to that surface and are then removed from the simulation. Secondary electrons are emitted by the dielectric walls following a linear SEE yield law, $\delta_s(\mathcal{E}_{eWt}) = \mathcal{E}_{eWt}/\mathcal{E}_c$, with \mathcal{E}_{eWt} the impacting electron energy and $\mathcal{E}_c = 50$ eV the material cross-over energy. Secondary electrons are sampled from a Maxwellian flux VDF with an average energy of 0.4 eV. At the metallic anode wall, no SEE is considered. Additionally, electrons are injected from the cathode such that continuity of discharge current, I_d , flowing between anode and cathode, is satisfied at any instant of the simulation. Electrons generated at the cathode are sampled from a Maxwellian flux VDF with a mean energy of 4.5 eV and the injected flux distribution over the neutralizer boundary is assumed uniform.

Neutrals, n , are described as a background fluid and follow a simplified depletion law that conserves the total mass flow and accounts for both, volumetric ionization and recombination of ions reaching the thruster walls⁷. This approach avoids simulating long time-scales associated to the slow neutral dynamics and allows reaching steady-state solutions of the discharge.

Collisions are implemented using standard Monte Carlo Collision (MCC) algorithms. The simulation includes elastic, excitation and ionization $e-n$ events, while ions are considered collisionless. The collisional cross-sections are retrieved from the Biagi database¹⁷ available in LXCat. Due to the axial-radial nature of the simulation, azimuthal instabilities inducing cross-field electron transport cannot be resolved. Alternatively, an empirical model is used, and their effect is included as an isotropic anomalous collisionality of the form $\nu_{ano} = \alpha_{ano} \omega_{ce}$, with $\omega_{ce} = eB/m_e$ the electron cyclotron frequency and α_{ano} a fitting function. Here, the anomalous transport map of Ref. 18, calibrated to reproduce typical values of the PPS5000, has been applied.

The magnetic field, \mathbf{B} , is static and externally applied. The 2D map of the imposed magnetic topology is shown in Fig. 2(a), including the field magnitude and contours for the magnetic field lines. As it can be observed, the magnetic field is radially asymmetric. The

topology is almost radial near the channel exit but features a large curvature in the inner part of the channel. We can distinguish between magnetic field lines connecting the two lateral walls (with a moderate curvature) and those joining one of the lateral walls with the anode (with large curvature). The magnetic separatrix that depicts the approximate transition between these two regions is plotted in red in Fig. 2(a). It intersects the inner wall at $z \approx 8.46$ mm, the outer wall at $z \approx 13.65$ mm, and the anode wall at $r \approx 62.9$ mm, bounding the region of strong magnetic field curvature. Additionally, the intersection of the magnetic separatrix with the anode surface also coincides with a point where the magnetic field becomes practically null, $\min(B_A) \approx 0.2$ G. Axial profiles of the magnetic field norm along the mean radius, and at $r = 62.9$ mm are plotted for comparison in Fig 2(b).

In the electrostatic approximation the electric field is $\mathbf{E} = -\nabla\phi$ and the electric potential, ϕ , is obtained from the Poisson equation

$$\frac{\partial^2\phi}{\partial z^2} + \frac{\partial^2\phi}{\partial r^2} + \frac{1}{r}\frac{\partial\phi}{\partial r} = \frac{e(n_e - n_i)}{\epsilon}, \quad (2)$$

where ϵ is the electric permittivity and n_e , n_i are the electron and singly charged ion densities respectively. Dirichlet boundary conditions are imposed at the anode ($\phi_A = 300$ V) and cathode surfaces ($\phi_N = 0$), fixing the discharge potential $V_d = \phi_A - \phi_N$, and Neumann conditions are applied at the dielectric walls,

$$\epsilon\mathbf{E} \cdot \mathbf{1}_n = \sigma(t) \equiv - \int_0^t \mathbf{j} \cdot \mathbf{1}_n dt, \quad (3)$$

where: $\mathbf{1}_n$ is the unit vector perpendicular to the surface and pointing towards the plasma, σ is the surface charge density, and \mathbf{j} is the electric current density. Note that at the steady-state Eq. (3) implies a local zero current collected at the dielectric walls. The numerical implementation makes use of finite differences for the calculation of ϕ and \mathbf{E} at the mesh nodes.

The strict numerical constraints on the cell size and time step imposed by the Debye length and the inverse plasma frequency respectively are relaxed by using an augmented permittivity $\epsilon = f_D^2\epsilon_0$, where ϵ_0 is the vacuum permittivity. This allows a reduction of a factor f_D^3 in computational cost without a significant distortion of the steady-state solution as long as the Debye length remains the smallest length scale of the problem⁷. Here we apply $f_D = 12$, a common value used in previous works in the literature^{11,19}.

Regarding numerical parameters, a square mesh with cell size $\Delta z = \Delta r = 200$ μm has been employed. The simulation time-step is $\Delta t = 15$ ps and the total simulated time is 60 μs . The simulation shown here was run using 20 cores on a workstation with 2 sockets, each one with 20 cores Intel(R) Xeon(R) Gold 6230 CPU @ 2.10 GHz. The simulation time is approximately one week.

III. SIMULATION RESULTS AND DISCUSSION

The simulation starts with a filled domain and Maxwellian VDFs for electrons and ions. Initially, identical particle densities and temperatures for electrons and ions are considered, with $n_{e0} = n_{i0} = 4 \cdot 10^{17}$ m⁻³ and $T_{e0} = T_{i0} = 1$ eV. During the initial transient, electrons and ions reaching the walls build up surface charge. Then, Debye sheaths are formed, the electric current to the wall becomes zero and the surface charge stabilizes [see Eq. (3)]. After approximately 40 μs , steady-state is reached. Hereon, only the stationary plasma response will be discussed. In order to mitigate the PIC related noise, stationary results are time-averaged over the last 7.5 μs of the simulation (i.e. 500000 time-steps). At steady-state, the number of simulated particles per species is over one million. At steady-state, the discharge current is $I_d \approx 18$ A, which yields a discharge power of $P_d \approx 5.5$ kW. Those figures agree well with the expected operation of a 5kW-class HET that we are aiming to simulate.

A. Description of the stationary response

The 2D maps of relevant macroscopic magnitudes are shown in Fig. 5: (a) electric potential, ϕ ; (b) electron temperature, T_e ; (c) electron density, n_e ; (d) azimuthal electron current, $j_{\theta e}$; (e) and (f) longitudinal ion and electron current densities respectively. For a given vector magnitude, the longitudinal part is defined as $\tilde{\Gamma} = \Gamma - \Gamma_\theta \mathbf{1}_\theta$. In this paper, the analysis focuses on the thruster channel. Previous simulations¹⁴ have shown that the impact of the size of the near plume on the plasma solution inside the HET channel is negligible.

The main differences with respect to Ref. 7 are triggered by the magnetic topology. The local plasma behavior within the channel reveals significant differences between the regions upstream and downstream the magnetic separatrix. The near-anode plasma, bounded by the anode surface and the magnetic separatrix, features a complex 2D response which is analyzed in Section VI. The region downstream the magnetic separatrix follows the usual trends expected in a HET discharge. At the central section of the HET channel, there is the ionization region, with maxima in n_e and ϕ . Near the exit, there is the acceleration region characterized by a mainly axial acceleration of ions and a decreasing n_e . In this region the magnetic field is almost radial and the macroscopic plasma response follows the known trends from 1Dz/1Dr fluid models²⁰. The electrons injected from the cathode (i.e. the downstream plume boundary) are heated by Joule effect in the near plume. The maximum in T_e is reached near the thruster exit, which approximately coincides with the local maxima of \mathbf{B} and \mathbf{E} . In the thruster channel, the electron temperature decreases due to energy losses to the walls and inelastic collisions.

The electron energy flux vector can be expressed as the

addition of four different contributions

$$\mathbf{P}_e'' = \mathbf{h}_e + \mathbf{q}_e + \mathbf{U}_e + \mathbf{\Pi}_e, \quad (4)$$

with $\mathbf{h}_e = (5/2)n_e T_e \mathbf{u}_e$ the enthalpy flux, \mathbf{q}_e the heat flux, $\mathbf{U}_e = m_e u_e^2 n_e \mathbf{u}_e / 2$ the flux of fluid flow energy and $\mathbf{\Pi}_e = (\bar{\rho}_e - p_e \bar{I}) \cdot \mathbf{u}_e$ the term caused by the fact that the electron pressure tensor deviates from an isotropic gyrotropic one. The different terms in Eq. (4) are plotted in Fig. 6 (a), (b), (c) and (d) respectively. The electron energy flux vector follows complex 2D patterns. In most of the channel, the enthalpy and heat flux clearly dominate. However, \mathbf{U}_e and $\mathbf{\Pi}_e$ become relevant near the anode surface. Moreover, the heat flux does not follow a standard Fourier law, see Fig. 4.

B. Radial profiles

Figure 7 plots profiles of electric potential, plasma density and electron temperature at five different axial locations. For a better comparison, density and potential profiles are presented in non-dimensional form, $n_{i,e}/\bar{n}_e$ and $e(\phi - \phi_M)/\bar{T}_e$, where M refers to the mean channel radius $r_M = (r_{W1} + r_{W2})/2$ and a bar over a magnitude indicates that it is a radially averaged value, i.e. $\bar{G}(z) = (r_2^2 - r_1^2)^{-1} \int_{r_1}^{r_2} 2r G(z, r) dr$. Radial profiles near the thruster exit resemble those obtained with a 1Dr PIC model of the discharge assuming a purely radial magnetic field^{21,22}. In this region of quasiradial magnetic field, macroscopic magnitudes exhibit radial asymmetries that were absent in the quasiplanar scenario with purely radial magnetic field analyzed in Ref. 7. Radial asymmetries are induced by cylindrical effects on the discharge and the magnetic field topology. Moving towards the center of the channel, the magnetic curvature increases and the profiles follow the same qualitative trends as in Ref. 12 for an anode-pointing magnetic lens configuration. The radial profile of shows large gradients of n_e , with a peak plasma density at $r = 6.29$ cm and low plasma density near the walls. The 2Dzr model is no longer limited to moderately curved magnetic fields and allows to overcome the limitations of the 1Dr model. Close to the anode, upstream the magnetic separatrix, the results do not resemble those obtained in previous works using 1Dr models of the discharge and require further analysis. Still, the peak plasma density is consistently located at $r = 6.29$ cm and the strong axial component of \mathbf{B} leads to sharp radial changes in n_e .

C. Velocity distribution functions at the plasma bulk

The PIC model implementation allows to calculate velocity distribution functions of electrons and ions at different locations to get further insights of the kinetic response. Figure 9 plots the normalized 1V electron VDFs⁷ along at $r = 6.29$ cm and different axial positions inside

the HET channel. These VDFs are defined as

$$\begin{aligned} \hat{f}_e^{(z)}(v_z) &= \iint_{-\infty}^{\infty} f_e(\mathbf{v}) dv_r dv_\theta \\ \hat{f}_e^{(r)}(v_r) &= \iint_{-\infty}^{\infty} f_e(\mathbf{v}) dv_z dv_\theta \\ \hat{f}_e^{(\theta)}(v_\theta) &= \iint_{-\infty}^{\infty} f_e(\mathbf{v}) dv_z dv_r \end{aligned} \quad (5)$$

The VDFs are plotted in logarithmic scale in the 'y' axis and the 'x' axis represents the directional electron energy $m_e v_{xe} |v_{xe}| / 2$, for $x = z, r, \theta$. Therefore, a Maxwellian VDF yields a line with constant slope and the wider the VDF (larger velocity dispersion), the higher the temperature. The relative shapes of the VDFs in Fig. 9 show that the peak electron temperatures are reached near the thruster exit, in agreement with Fig. 5(b). At $z = 1.5$ cm and $z = 2.5$ cm the axial and azimuthal VDF are almost identical with an approximately linear slope, yielding $T_{ze} \approx T_{\theta e}$. The weak asymmetry between $\hat{f}_e^{(z)}$ and $\hat{f}_e^{(\theta)}$ is due to $u_{ze} \ll u_{\theta e} \ll c_e$. The high energy tails of the radial VDF are depleted due to wall collection and the weak collisionality. This reduces the radial temperature and leads to temperature anisotropy with $T_{re} < T_{ze} \approx T_{\theta e}$. Qualitatively, this result is identical to those obtained from previous 1Dr models of the acceleration region of the discharge^{21,22} and 2Dzr models⁷ assuming a purely radial magnetic field. As we move towards the central part of the channel the magnetic curvature increases. At $z = 0.9$ cm it can be observed a larger replenishment of the radial VDF. This result is in agreement to previous works with 1D models accounting for the magnetic field curvature^{12,13}, which explained this effect due to the larger mixing between the radial and axial components of the velocity as a consequence of the magnetic field shape. At $z = 0.6$ cm the low wall losses [see Section V] and high curvature of the magnetic field leads to $\hat{f}_e^{(r)}$ that does not present depleted tails. The larger asymmetry between $\hat{f}_e^{(\theta)}$ and $\hat{f}_e^{(z)}, \hat{f}_e^{(r)}$ is the signature of a greater $u_{\theta e}$. Closer to the anode, at $z = 0.3$ cm, an asymmetric $\hat{f}_e^{(z)}$ can be observed, with more electrons traveling with $v_z < 0$ than in the opposite direction. This is a consequence of the collection of electrons by the anode wall, as previously observed in Ref. 7, which leads to a lower T_{ze} .

Figure 23 depicts the normalized 1V VDFs of ions. In general, the peak of the axial ion VDF moves towards higher positive axial velocities from the anode to the exit. This is, the ion population is accelerated downstream in the HET channel, as expected. Moreover, the VDF shows dispersion in ion velocities and the resulting VDF differs much from a Maxwellian. This is indeed normal for a collisionless species. Ions are generated via $e - n$ ionization events and are then accelerated by the electric field. Thus, the ion VDFs is composed of a newborn ions, which populates the low energy region of the VDF, and fast ions that have been accelerated by the electric field. Depending on the local intensity of ionization and

the amount of accelerated ions, two-peaked VDFs can be found, as shown at $z = 0.9$ cm.

IV. MACROSCOPIC BALANCES

A. The electron momentum equation

The radial response is determined by the radial momentum equation. The dominant contributions to this equation are

$$0 \simeq -\frac{\partial p_{rre}}{\partial r} - en_e E_r + j_{\theta e} B_z. \quad (6)$$

Where other terms, including inertia, temperature anisotropy and collisions have been found negligible in the bulk plasma. Therefore, it reduces to a balance among the electron pressure ($-\partial p_{rre}/\partial r$), electric ($-en_e E_r$) and magnetic ($j_{\theta e} B_z$) forces. The different terms in this equation are plotted in Fig. 16 at five axial sections of the HET channel. At each axial section the electric and pressure forces change sign, being the former a confining force (pushing the electron fluid away from the walls) and the latter an expanding force (pushing the electron fluid towards the walls). The magnetic force can be either electron expanding or confining depending on the magnetic field curvature. For a magnetic field curved towards the anode, the magnetic force has a confining character, while in the opposite configuration the magnetic force has an electron expanding character¹². Near the anode the electron-confining magnetic force is balanced by the pressure force and the electric force remains small. This agrees with both, the radial plateau of ϕ , and the steep radial gradient of n_e in the quasineutral plasma [see Fig. 7(a) and (b) for $z < 1.0$ cm]. As the curvature of the magnetic field decreases in the thruster channel, B_z becomes smaller, and the magnetic term in the radial momentum equation becomes less relevant. As a consequence, the radial momentum equation approximately simplifies to a balance between the expanding pressure force and the confining electric force. Finally, it is worth noting that at $z = 2.5$ cm the magnetic force does not change sign inside the channel and it is always pushing the electron fluid towards the inner wall. This leads to higher particle fluxes to the inner wall than to the outer wall [see Fig. 14].

The azimuthal electron current, $j_{\theta e}$, is determined by the axial momentum equation

$$0 \simeq -\frac{\partial p_{zze}}{\partial z} - en_e E_z - j_{\theta e} B_r. \quad (7)$$

The radially averaged contributions to Eq. (7) are plotted in Fig. 17(a), showing a similar trends as in Ref. 7. Collisional effects and M_{rze} are subdominant with respect to the strong electron pressure ($-\partial p_{zze}/\partial z$) and electric force ($-en_e E_z$). The effect of electron inertia is small and it is only noticeable at the anode sheath. Thus, the solution of this equation is quite standard and the results

are consistent for radial and curved magnetic field topologies. The local maxima in the electric and magnetic force contributions are due to the local features of the plasma response in the near anode region, to be analyzed in more detail in the Section VI.

The azimuthal electron momentum equation determines the axial electron current towards the anode. The main terms involved in this balance are

$$0 \simeq -\frac{\partial M_{z\theta e}}{\partial z} + j_{ze} B_r - j_{re} B_z + F_{col,\theta e}. \quad (8)$$

The radially averaged contributions to Eq. (8) are plotted in Fig. 17(b). Here, the dominant terms are much smaller (typically 2 orders of magnitude) than in the axial momentum equation. Near the thruster exit B_z is small and $\partial M_{z\theta e}/\partial z$ leaves a negligible contribution to the balance, i.e. the drift-diffusive electron solution is found $j_{ze} B_r \simeq -F_{col,\theta e}$. Conversely, near the anode, all the terms in the Eq. (8) become relevant. The non-negligible contribution of the term $\partial M_{z\theta e}/\partial z$ in the azimuthal electron momentum equation is known as Finite-Larmor-Radius (FLR) effect. Other kinetic studies, 1Dz²³ and 2Dzθ⁷, seem to point towards the key role of FLR effects in the azimuthal momentum balance near the anode. This was also the case in our previous work⁷ with a purely radial magnetic field and lacking $e - n$ elastic collisions. Here, we are including $e - n$ collisions and the magnetic field features a large axial component near the anode, and yet FLR effects seem to be locally important. Nonetheless, we do not claim that this behavior is universal in HET physics. We acknowledge that the influence of FLR effects strongly depends on local plasma properties and requires a precise characterization of both electron-neutral collisionality and anomalous diffusion near the anode.

B. Continuity equation

The radially integrated steady-state current balance for electrons and ions can be expressed as

$$\frac{dI_{zs}}{dz} = \frac{dI_{prod}}{dz} - \frac{dI_{rs}}{dz}, \quad s = i, e, \quad (9)$$

with I_{zs} the axial current, dI_{prod}/dz the rate of current production, and dI_{rs}/dz the rate of current losses to the lateral walls. Figure 15(a) plots the different contributions to this balance. Near the anode, the plasma losses to the walls are very small; therefore, all the plasma production due to ionization contributes to the axial current. Conversely, near the thruster exit ionization compensates plasma losses to the lateral walls and the axial current is approximately constant.

Previous 1Dz models^{20,24?} describe wall losses as

$$\frac{1}{A} \frac{dI_{rs}}{dz} = e \bar{n}_e v_w, \quad (10)$$

with \bar{n}_e the average plasma density in the cross section and ν_w the wall collision frequency, defined as²⁴

$$\nu_w = \tilde{\nu}_w \frac{2\pi r_M}{A} \bar{c}_s, \quad (11)$$

with $\bar{c}_s = \sqrt{T_e/m_i}$ the radially averaged sonic speed for ions and $\tilde{\nu}_w$ is a phenomenological parameter to be fitted. Such parameter is typically assumed constant and Refs. 24? take $\tilde{\nu}_w = 0.17$. The 2D PIC model allows to calculate the local value of $\tilde{\nu}_w(z)$ from the kinetic results, depicted in Fig. 15(b). Downstream the magnetic separatrix $\tilde{\nu}_w \sim O(1)$; However, upstream the magnetic separatrix, this value is reduced between one and two orders of magnitude. Thus, the magnetic field curvature affects much the value of $\tilde{\nu}_w$.

V. PLASMA-WALL INTERACTION

Figure 14 depicts local wall interaction magnitudes along the inner (left column) and outer (right column) dielectric walls showing: (a), (b) ion current density to the wall j_{riW} , electron current density to the wall j_{reWt} , and electron current density from the wall (SEE) j_{reWF} ; (c), (d) ion energy flux to the wall P''_{riW} , electron energy flux to the wall P''_{reWt} , and electron (SEE) energy flux from the wall P''_{reWF} ; and (e), (f) ion energy to the wall \mathcal{E}_{iW} , electron energy to the wall \mathcal{E}_{eWt} , and electron (SEE) energy from the wall \mathcal{E}_{eWF} . From Fig. 14(a) and (b) it can be confirmed that, at steady state, the dielectric walls are locally current free. The particle fluxes to the lateral walls in the region bounded by the anode and the magnetic separatrix is several orders of magnitude smaller than in the rest of the channel. A similar behavior is found in the energy fluxes, as shown in Fig. 14(c) and (d). However, the electron impact energy, in Fig. 14(e) and (f), is higher upstream the magnetic separatrix than in other regions of the channel. This implies that electrons reaching the walls in that location are more energetic.

Table II gathers total currents and powers at the lateral walls, computed as integrals of the profiles in Fig 14. The inner and outer lateral walls present asymmetries in the current and power deposition figures. In particular, we observe higher electron and ion currents to the inner wall although the outer wall has larger surface area (the relation between the inner and outer wall surface areas is $r_{W2}/r_{W1} \simeq 1.41$). This is in agreement with the asymmetries in the electron density 2D map and radial profiles shown in Figs. 5(c) and 7(b), respectively, revealing consistently higher densities near the lower wall. On the contrary, we find a higher emission of secondary electrons from the outer wall. In absolute terms, the current of SEE generated at the lateral walls are $|I_{eW1f}| = 4.04$ A and $|I_{eW2f}| = 4.62$ A. In relative terms, the ratio between the current of secondary electrons emitted by the wall with respect to the current of electrons reaching reaching the wall yields $\delta_{s1} \simeq 0.52$ and $\delta_{s2} \simeq 0.71$. This means

that the average energy of electrons reaching the outer wall is higher than those collected at the inner wall. This results in a higher electron power deposition at the outer wall. SEE from the dielectric material promotes power losses to the walls, since secondary electrons are much colder than electrons reaching the thruster walls.

Figure 12(a) shows the local distribution of ion and electron current densities to the metallic anode wall. The radial position where particle fluxes to the anode are maxima coincides with the location where the magnetic separatrix intersects the anode, i.e. $r = 6.29$ cm. The integrated values in Table II show that the ion and electron currents collected at the anode are $I_{iA} \simeq 0.29$ A and $I_{eA} \simeq 18.71$ A. In normal operation it is desirable that the anode current is dominated by electrons; however, some ions must reach the anode surface to ensure plasma attachment and avoid sheath reversal?. Here, the fraction $|I_{iA}|/|I_{eA}| \simeq 1.5\%$ is larger than that obtained in Ref. 7 for a radial magnetic field at the anode. Standard theory predicts that the anode sheath vanishes for $|I_{iA}|/|I_{eA}| \leq 0.5\%$ for singly charged cold xenon ions²⁵. Contrary to results in Ref. 7, a normal electron-repelling Debye sheath is formed and no anode sheath reversal is observed. Nonetheless, the potential drop at the anode sheath is mild, ~ 3 V. This justifies the low average ion impact energy at the anode $\mathcal{E}_{iA} \simeq 6$ eV, shown in Fig. 12(b). Conversely, electrons reach the anode with a higher average energy, $\mathcal{E}_{eA} \simeq 20$ eV. This is a consequence of the local features of the electron VDF near the anode. Fig 13 shows 1Vz electron VDFs at $z = 0.3$ cm at three different radial positions. The VDFs deviate largely from a Maxwellian and reveal the presence two main electron populations. First, there is a low energy population coming from local ionization. Second, there is a tail of high energy electrons directed towards the anode. The high energy region of the VDF presents a similar slope at different radial locations. This is in line with the relatively high and uniform electron impact energy at the anode wall.

VI. ANALYSIS OF THE NEAR-ANODE REGION

Figure 11 zooms in the region that extends from the anode to $z = 1.5$ cm, where the magnetic field features a large curvature. The macroscopic variables in this area are strongly affected by the magnetic topology and the magnetic separatrix acts as boundary between the different plasma regions. Upstream the magnetic separatrix the magnetic field features a large curvature and partially shields the lateral dielectric walls. This prevents most of magnetized electrons to reach this region, since they cannot easily cross the separatrix. Consequently, the electron density drops about 2 orders of magnitude across the separatrix, as shown in Fig. 11(a). This agrees with the low electron particle and energy fluxes to the lateral walls, upstream the magnetic separatrix, as presented in Fig. 14. Electron streamlines, shown in

Fig. 11(f) also show this behavior. The lateral walls of the thruster are dielectric, and therefore, at steady-state, they cannot collect net electric current from the plasma, i.e., $|j_{rew}| = |j_{riw}|$ locally. Since $|j_{rew}| \approx 0$, the dielectric condition implies $|j_{riw}| \approx 0$, so that very few ions must reach the wall. To fulfill it, the electric field in the plasma self-adjusts to regulate the local flux of unmagnetized ions to the walls. At the outer wall, the electric potential grows from the plasma to the dielectric wall [see Fig. 8(a)]. This is contrary to the case of a classical electron repelling sheath and leads to local electric field reversal i.e. electron attracting and ion repelling, as shown in Fig. 11(d). The local electric field accelerates ions mainly along the axial direction yielding ion streamlines flowing almost parallel to the walls, as depicted in Fig. 11(e). The inspection of the ion VDFs, in Fig. 19, confirms the axial acceleration of ions. At $z = 0.90$ cm the radial ion VDF shows reflection of low energy ions as a consequence of the local electric field reversal.

Additionally, the electric field work is the main source of energy for electrons. Fig. 11(g) shows the 2D map of power deposited by the electric field per electron particle, $-e\mathbf{u}_e \cdot \mathbf{E} = j_e \cdot \mathbf{E}/n_e$. It features peaks near the lateral walls, immediately upstream the magnetic separatrix. Such peaks trigger local maxima in T_e , as shown in 11(h). This local heating of electrons can be also observed from the electron VDFs, in 18 showing populated high energy tails. At the same time, in this region electrons deviate from the drift-diffusive postulate and show $m_e u_e^2/T_e > 1$, as shown in Fig. 11(i). The fluid electron velocity dominated by $u_{\theta e}$, which suffers a steep change across the magnetic separatrix [see Fig. Fig. 11(j)]. The local analysis of the different term the axial momentum equation [Eq. (7), in Figs. 11(k) and (l)] reveal that the increase of $u_{\theta e}$ is mainly driven by the term $\partial M_{zze}/\partial z$; which becomes large due to the sharp change in n_e across the magnetic separatrix [in Fig. 11(a)].

This unconventional plasma response near the anode is highly dependent on the local mobility of electrons across magnetic field lines. A simulation with higher anomalous diffusion reveals a more conventional response in plasma magnitudes near the anode and a potential map that monotonically decreases towards the dielectric walls. Therefore, a self-consistent characterization of this region requires a 3D kinetic description of the plasma discharge, that takes into account azimuthal instabilities, wall collection and axial plasma transport effects.

VII. CONCLUSION

AM: TBD:

The 2D axial-radial PIC model of Ref. 7 (PICASO) has been improved to analyze more realistic HET discharges, considering cylindrical effects and a curved magnetic field topology. Electrons and singly charged ions are treated as two populations of macroparticles. Alternatively, neutrals

are modeled as a background fluid. Ionization, excitation and elastic electron-neutral collisions are simulated with MCC algorithms. An empirical model for anomalous diffusion is included to account for electron transport induced by azimuthal instabilities. Acceleration techniques, such as a steady-state law for neutrals and an augmented vacuum permittivity, have been used to reduce the required computational cost. The reference case simulates a virtual 5 kW class HET, which resembles PPS@5000. The magnetic topology features a large curvature near the anode and is almost radial near the exit. The time-evolution of currents to different domain boundaries shows convergence converge and steady-state solution is analyzed. Near the thruster exit, the results are similar to simulations with a purely radial magnetic field⁷. Near the anode the plasma features a complex 2D response. The approximate transition between the two regions is marked by a magnetic separatrix. Simulation results indicate that that the curved magnetic field topology near the anode effectively reduces particle and energy fluxes to the lateral dielectric walls. The calculation of the wall interaction parameter $\tilde{\nu}_w$ used in 1Dz models of the discharge^{20,24} shows a strong dependence with the magnetic field curvature and justifies the value of $\tilde{\nu}_w = 0.17$ considered in previous works. Simulation results suggest that the normal Debye sheath may not be present for a grazing magnetic incidence. Near the anode, radial profiles show a plasma density concentrated in the channel center, away from the walls. The analysis of the radial momentum equation reveals that it consists of a balance between the pressure gradient, electric and magnetic force mainly. Near the thruster anode the strong curvature of the magnetic field induces a radially confining magnetic force which is compensated by the expanding pressure gradient term, while the electric force diminishes. This explains the observed trends in the radial profiles of macroscopic magnitudes. The axial electron momentum balance determines the azimuthal electron current, which is a result of $E \times B$ and diamagnetic drifts. The azimuthal electron momentum equation determines the axial electron current and shows an important contribution of FLR effects near the anode region. The analysis of other simulation cases reveals that there is little difference in the results if a constant anomalous diffusion parameter is used instead of a step-out profile. However, the amount of anomalous diffusion inside the HET channel is crucial and affects significantly the plasma response.

ACKNOWLEDGMENTS

This work has been supported by the R&D project HEEP (PID2022-140035OB-I00) funded by MCIN/AEI/10.13039/501100011033 and by “ERDF A way of making Europe”.

The authors thank E. Bello-Benítez for his contribution to the development of the original version of the code.

Appendix A: Effect of the augmentation factor of the vacuum permittivity

AM: Wall interaction, axial profiles and near anode maps

Appendix B: Effect of the number of simulated particles

AM: Wall interaction and axial profiles

Appendix C: Estimation of the numerical thermalization frequency

Estimation of the number of macroparticles per Debye volume. Taking the reference values in Table I: $n_e = 3 \cdot 10^{18} \text{ m}^{-3}$, $\lambda_{De} = 230 \mu\text{m}$ and $r_M = 65.5 \text{ mm}$.

$$N_D \simeq 2\pi r_M \lambda_{De}^2 n_e / w_p \simeq 100 \quad (\text{C1})$$

The characteristic relaxation time τ_R due to numerical thermalization can be estimated as

$$\omega_{pe} \tau_R = \frac{2\pi N_D}{0.98} \left[1 + \left(\frac{\Delta x}{\lambda_D} \right)^2 \right] \simeq 1126 \quad (\text{C2})$$

Thus, the numerical thermalization equivalent frequency is

$$\frac{1}{\tau_R} = \omega_{pe} / 1126 = 7.22 \cdot 10^6 \text{ s}^{-1} \quad (\text{C3})$$

while the anomalous collision frequency is

$$\nu_{ano} = \alpha_{ano} \omega_{ce} = 5.29 \cdot 10^7 \text{ s}^{-1} \quad (\text{C4})$$

An estimation for the inverse of the radial transit time gives

$$1/\tau_r = \bar{c}_e / L_r = 1.35 \cdot 10^8 \text{ s}^{-1} \quad (\text{C5})$$

The use of an increased vacuum permittivity leads to a numerical thermalization time that is longer than other phenomena affecting the electron velocity distribution function.

REFERENCES

- ¹A. Ortega, I. Mikellides, M. Sekerak, and B. Jorns, Journal of Applied Physics **125** (2019).
- ²J. Perales-Díaz, A. Domínguez-Vázquez, P. Fajardo, E. Ahedo, F. Faraji, M. Reza, and T. Andreussi, Journal of Applied Physics **131**, 103302 (2022).
- ³J. Bittencourt, Fundamentals of plasma physics (Springer, Berlin, Germany, 2004).
- ⁴E. Ahedo, Journal of Electric Propulsion **2**, 2 (2023).
- ⁵F. Taccogna and L. Garrigues, Reviews of Modern Plasma Physics **3**, 12 (2019).
- ⁶E. Bello-Benítez, A. Marín-Cebrián, and E. Ahedo, “Effect of injection conditions on the non-linear behavior of the ECDI and related turbulent transport,” (2024), pre-print available at <https://arxiv.org/pdf/2405.08761.pdf>, arXiv:2405.08761 [physics.plasm-ph].
- ⁷A. Marín-Cebrián, E. Bello-Benítez, A. Domínguez-Vázquez, and E. Ahedo, Plasma Sources Science and Technology **33**, 025008 (2024).
- ⁸V. Kim, J. Propulsion Power **14**, 736 (1998).
- ⁹R. Hofer and A. Gallimore, in 38th Joint Propulsion Conference, AIAA 2002-4111 (Indianapolis, IN, 2002).
- ¹⁰J. Liu, H. Li, Y. Hu, X. Liu, Y. Ding, L. Wei, D. Yu, and X. Wang, Contributions to Plasma Physics **59**, e201800001 (2019).
- ¹¹D. Ma, D. Zeng, L. Wang, Y. Ding, L. Wei, H. Li, and D. Yu, Vacuum **180**, 109547 (2020).
- ¹²A. Marín-Cebrián, A. Domínguez-Vázquez, P. Fajardo, and E. Ahedo, Plasma Sources Science and Technology **31**, 115003 (2022).
- ¹³J. Miedzik, S. Barral, and D. Daniško, Physics of Plasmas **22**, 043511 (2015).
- ¹⁴A. Marín-Cebrián, E. Bello-Benítez, E. Ahedo, and A. Domínguez-Vázquez, in 38th International Electric Propulsion Conference, IEPC-2024-387 (Electric Rocket Propulsion Society, Toulouse, France, June 23-28, 2024).
- ¹⁵C. Birdsall and A. Langdon, Plasma Physics via Computer Simulation (Institute of Physics Publishing, Bristol, 1991).
- ¹⁶A. Domínguez-Vázquez, F. Cichocki, M. Merino, P. Fajardo, and E. Ahedo, Plasma Sources Science and Technology **27**, 104009 (2018).
- ¹⁷Biagi, S.F., “Cross sections extracted from PROGRAM MAG-BOLTZ, version 7.1 june 2004,” (2004), [Online; accessed 5-July-2021].
- ¹⁸A. Domínguez-Vázquez, J. Zhou, A. Sevillano-González, P. Fajardo, and E. Ahedo, in 37th International Electric Propulsion Conference, IEPC-2022-338 (Electric Rocket Propulsion Society, Boston, MA, USA, June 19-23, 2022).
- ¹⁹J. Szabo, N. Warner, M. Martinez-Sánchez, and O. Batishchev, Journal of Propulsion and Power **30**, 197 (2014).
- ²⁰E. Ahedo, J. Gallardo, and M. Martínez-Sánchez, Physics of Plasmas **10**, 3397 (2003).
- ²¹A. Domínguez-Vázquez, F. Taccogna, and E. Ahedo, Plasma Sources Science and Technology **27**, 064006 (2018).
- ²²A. Marín-Cebrián, A. Domínguez-Vázquez, P. Fajardo, and E. Ahedo, Plasma Sources Science and Technology **30**, 115011 (2021).
- ²³Y. Yamashita, R. Lau, and K. Hara, Journal of Physics D: Applied Physics (2023).
- ²⁴E. Bello-Benítez and E. Ahedo, Plasma Sources Science and Technology **32**, 115011 (2023).
- ²⁵E. Ahedo and D. Escobar, Physics of Plasmas **15**, 033504 (2008).

OTHER FIGURES AND TABLES

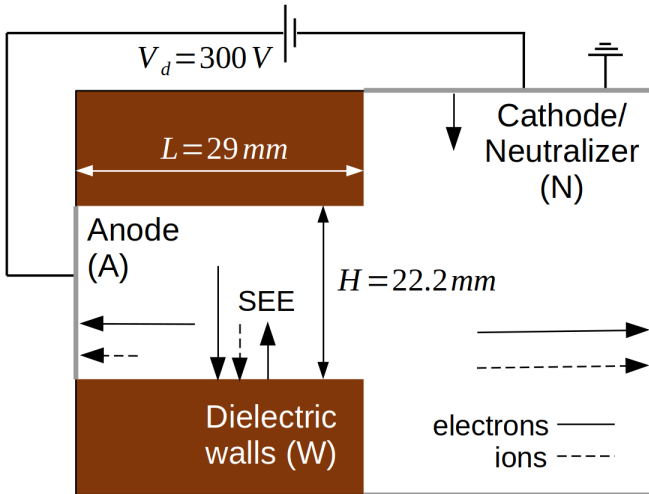


FIG. 1. Sketch of the simulation domain. Arrows indicate the expected direction of the electron (—) and ion (---) fluxes. The downstream plume boundary also acts as cathode/neutralizer, injecting electrons to satisfy continuity of the discharge current (between anode and cathode) at any instant.

Type	Description and symbol	Value and units
Physical system parameters	Channel inner radius, r_{W1}	54.5 mm
	Channel outer radius, r_{W2}	76.7 mm
	Channel length, L	29 mm
	Anode potential, ϕ_A	300 V
	Cathode potential, ϕ_N	0
	Mass flow, \dot{m}	17.59 mg/s
Surface interaction parameters	Wall cross-over energy, \mathcal{E}_c	50 eV
	SEE average emission energy, \mathcal{E}_{eWf}	0.4 eV
	Cathode average emission energy, \mathcal{E}_{eNf}	4.5 eV
Species settings	Initial plasma density, $n_{e0} = n_{i0}$	$4 \cdot 10^{17} \text{ m}^{-3}$
	Initial plasma temperature, $T_{e0} = T_{i0}$	1 eV
	Axial neutral velocity, u_{zn}	300 m/s
Characteristic plasma magnitudes	Debye length, λ_{De} (*)	230 μm
	Larmor radius, ρ_e	681 μm
	Inverse plasma frequency, ω_{pe}^{-1} (*)	123 ps
	Inverse gyrofrequency, ω_{ce}^{-1}	227 ps
Numerical parameters	Macroparticle weight, w_p	$6.59 \cdot 10^8$
	Grid spacing, $\Delta z = \Delta r$	200 μm
	Timestep, Δt	15 ps
	Simulated time, t_{sim}	60 μs
	Augmentation factor, f_D	12

TABLE I. Main input parameters for the 2Dzr PIC model. The characteristic plasma magnitudes have been calculated for $n_e = 3 \cdot 10^{18} \text{ m}^{-3}$, $T_e = 20 \text{ eV}$ and $B = 250 \text{ G}$. The Debye length and inverse plasma frequency, marked with an asterisk (*), are augmented by a factor f_D .

Description and symbol	Value and units
Discharge current, I_d	18.42 A
Ion current to the anode, $ I_{iA} $	0.29 A
Electron current to the anode, $ I_{eA} $	18.71 A
Ion current to the inner wall, $ I_{iW_1} $	3.71 A
Electron current to the inner wall, $ I_{eW_1t} $	7.75 A
SEE current from the inner wall, $ I_{eW_1f} $	4.04 A
Ion current to the outer wall, $ I_{iW_2} $	1.90 A
Electron current to the outer wall, $ I_{eW_2t} $	6.52 A
SEE current from the outer wall, $ I_{eW_2f} $	4.62 A
Discharge power, I_dV_d	5525 W
Ion power to the anode, P_{iA}	2 W
Electron power to the anode, P_{eA}	402 W
Ion power to the inner wall, P_{iW_1}	491 W
Electron power to the inner wall, P_{eW_1t}	202 W
SEE power from the inner wall, P_{eW_1f}	2 W
Ion power to the outer wall, P_{iW_2}	261 W
Electron power to the outer wall, P_{eW_2t}	231 W
SEE power from the outer wall, P_{eW_2f}	2 W

TABLE II. Current and power deposited at different surfaces.

	$z = 0.3$ cm	$z = 0.6$ cm	$z = 0.9$ cm	$z = 1.5$ cm	$z = 2.5$ cm
T_{re} [eV]	5.70	8.93	7.92	13.22	32.62
T_{ze} [eV]	5.21	8.90	7.92	13.53	33.91
$T_{\theta e}$ [eV]	6.84	7.68	7.62	13.58	34.02
T_e [eV]	5.92	8.51	7.82	13.44	33.52
c_e [10^6 m/s]	1.02	1.22	1.17	1.54	2.43
$u_{\theta e}$ [10^5 m/s]	7.61	7.66	3.01	1.39	3.60
u_{ze} [10^3 m/s]	-39.34	-13.74	-4.96	-1.76	-3.27
u_{re} [10^3 m/s]	-2.43	0.96	0.86	-0.36	-0.58

TABLE III. Temperature and fluid velocity values at $r = 6.29$ cm and different locations inside the HET channel.

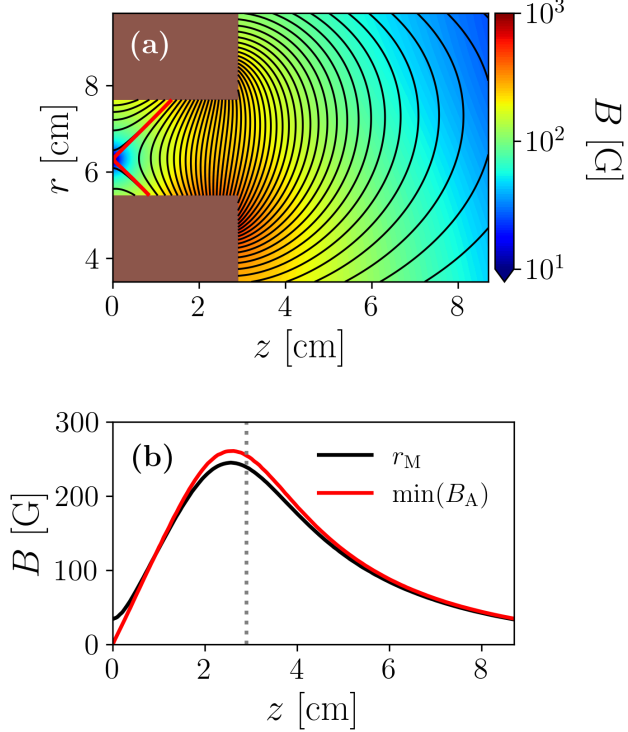


FIG. 2. Magnetic field topology: (a) shows a 2D plot of the imposed magnetic field, the black contours depict magnetic field lines, the red line represents the transition from magnetic field lines connecting the two lateral walls and those joining one of the lateral walls with the anode (b) plots axial profiles of the magnetic field magnitude at channel mean channel radius r_M and at the radial location of the minimum magnetic field at the anode $\min(B_A) \approx 0.2$ G at $r = 62.9$ mm. At $z \approx 8.46$ mm, the magnetic separatrix intersects the inner wall. At $z \approx 13.65$ mm, the magnetic separatrix intersects the outer wall.

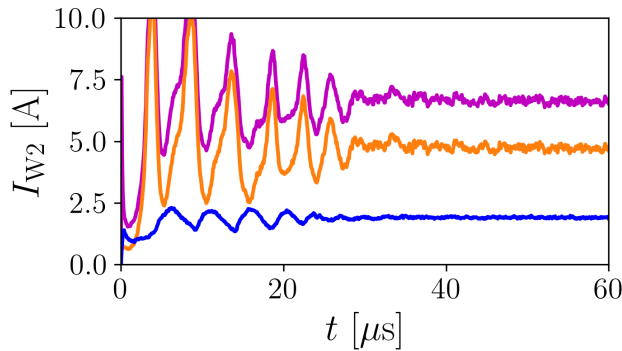


FIG. 3. Time evolution of the electron and ion currents to the outer wall: ions reaching the wall, $|I_{W2}|$ (blue); electrons reaching the wall, $|I_{eW2r}|$ (purple); and electrons emitted from the wall (SEE), $|I_{eW2f}|$ (orange).

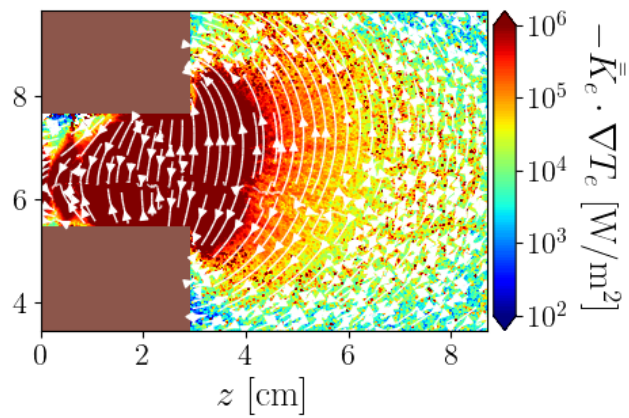


FIG. 4. Fluid heat flux

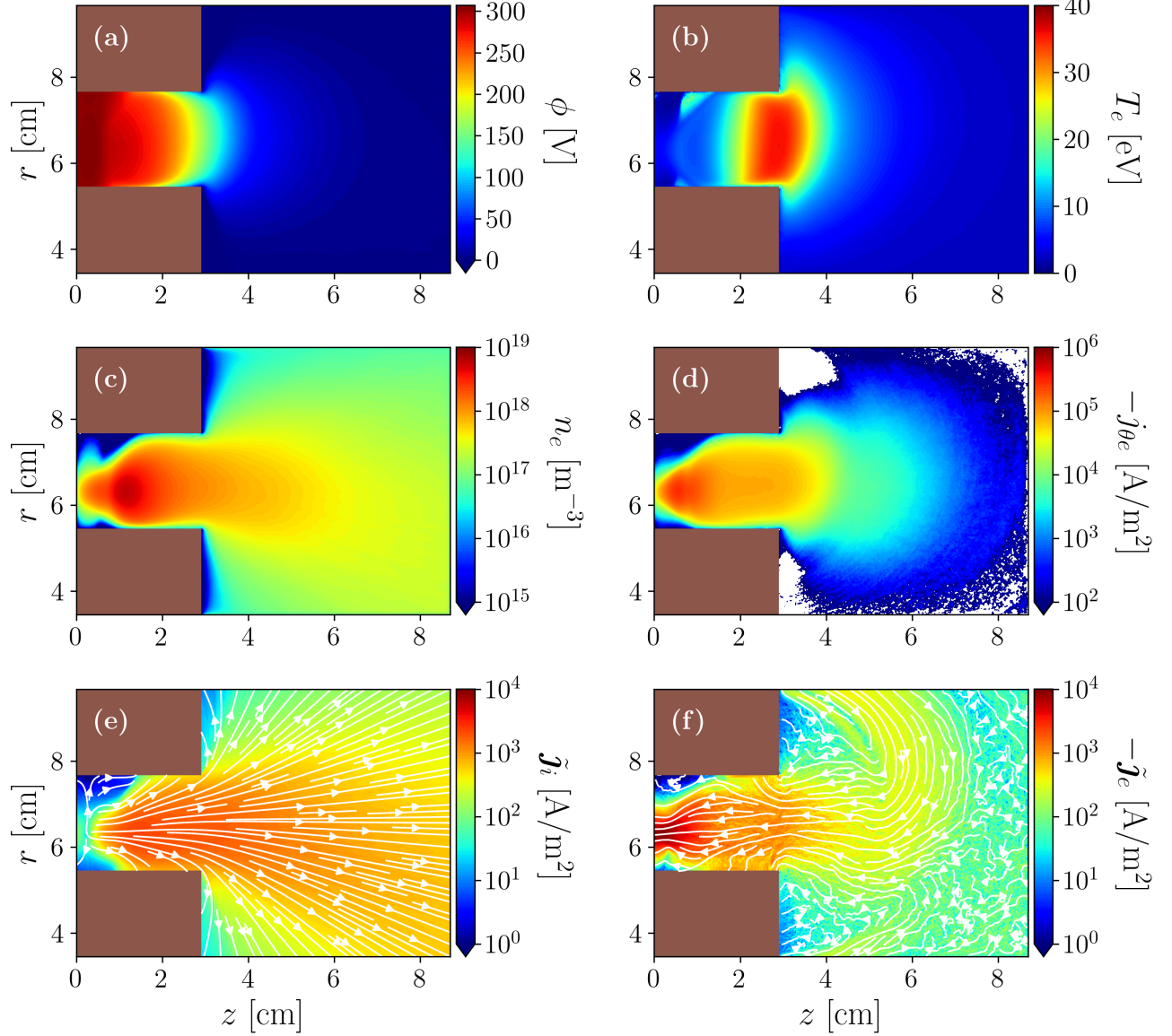


FIG. 5. Maps of the main macroscopic variables characterizing the reference case simulation at steady-state: (a) electric potential, (b) electron temperature, (c) electron density, (d) azimuthal electron current, (e) and (f) longitudinal ion and electron current densities respectively. **AM: Poner los puntos donde se calcula la VDF? AM: Quitar las corrientes de iones y electrones?**

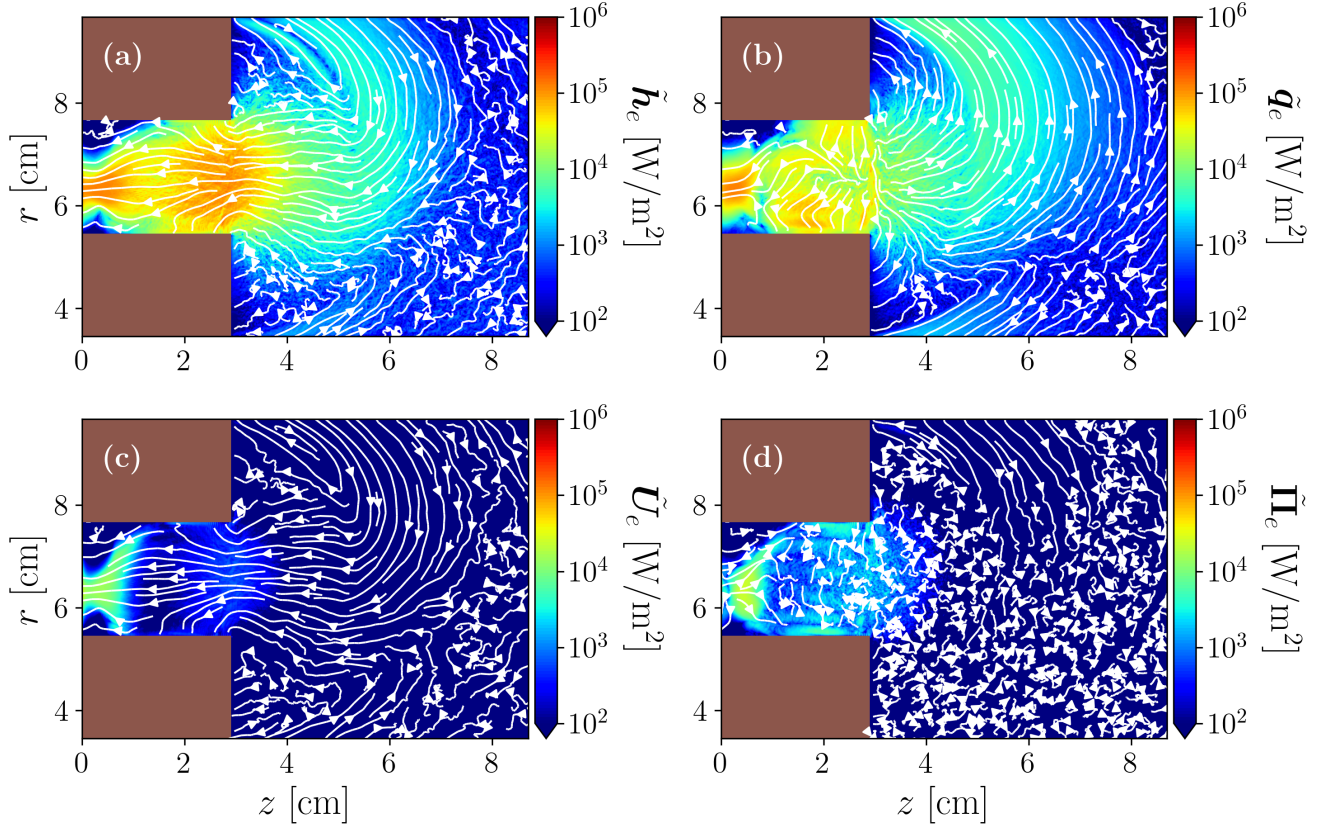


FIG. 6. Longitudinal electron energy flux vector contributions: (a) enthalpy flux, (b) heat flux, (c) fluid flow energy flux, and (d) gyrostress contribution.

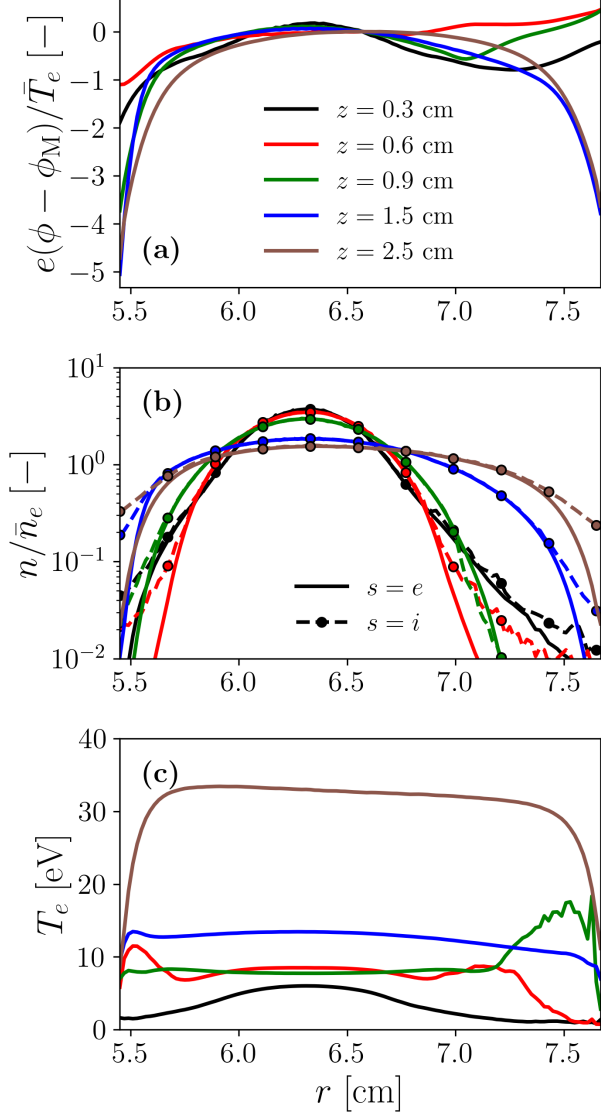


FIG. 7. Radial profiles of steady-state macroscopic variables for the reference case simulation at different axial locations: (a) non-dimensional electric potential, (b) non-dimensional ion and electron densities, (c) electron scalar temperature.

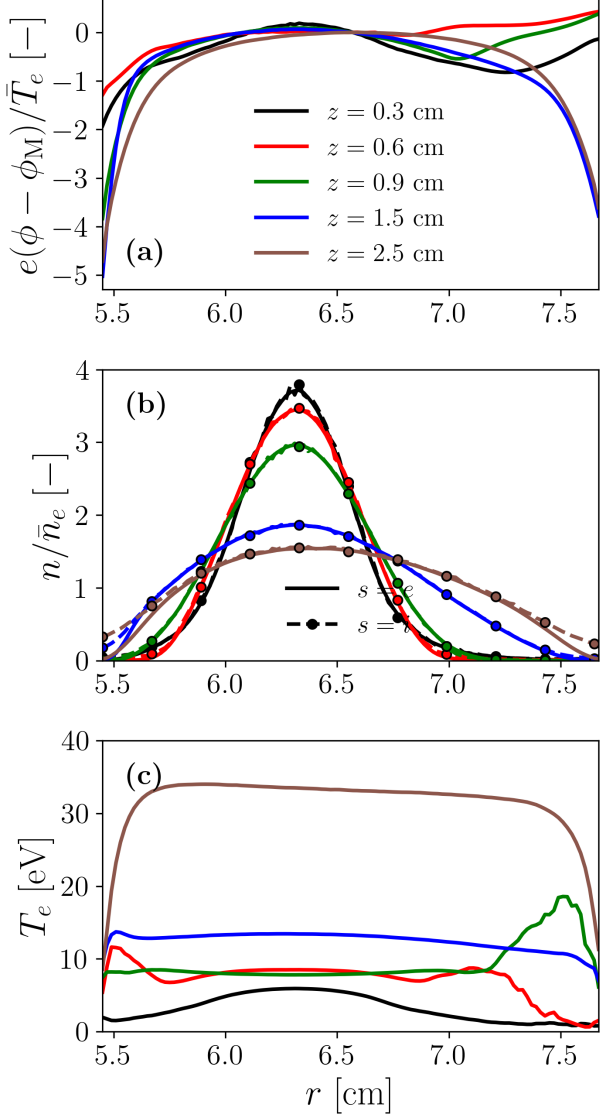


FIG. 8. Radial profiles of steady-state macroscopic variables for the reference case simulation at different axial locations: (a) non-dimensional electric potential, (b) non-dimensional ion and electron densities, (c) electron scalar temperature.

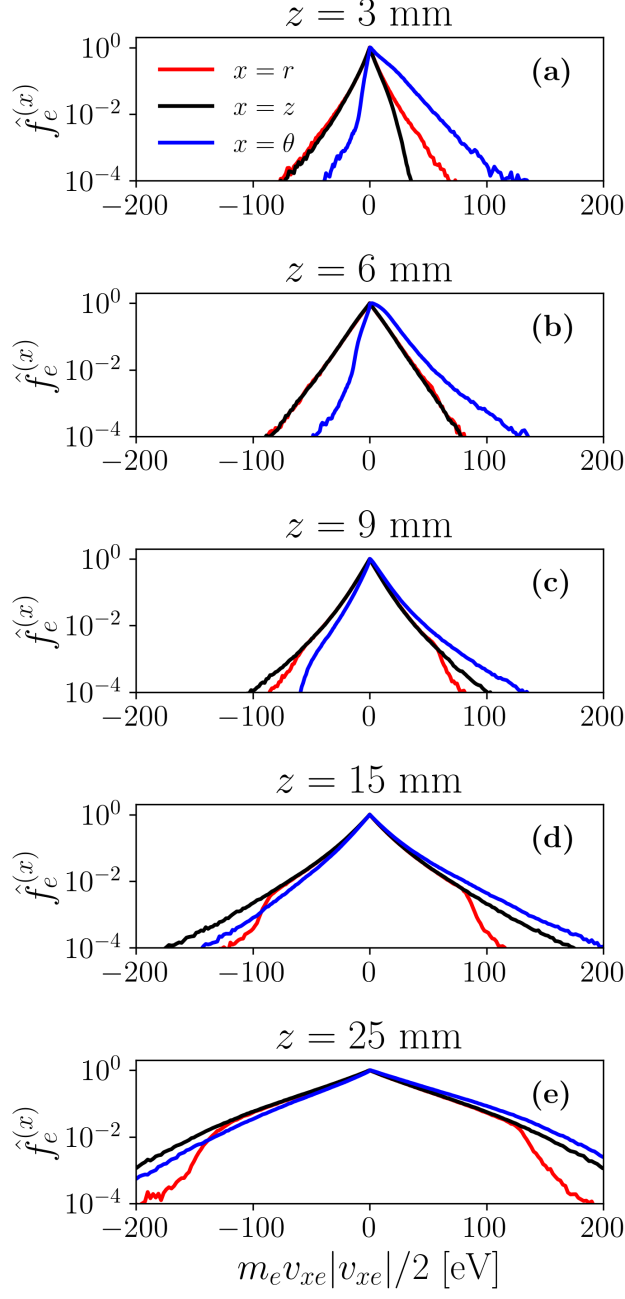


FIG. 9. Electron VDFs at different locations inside the HET channel.

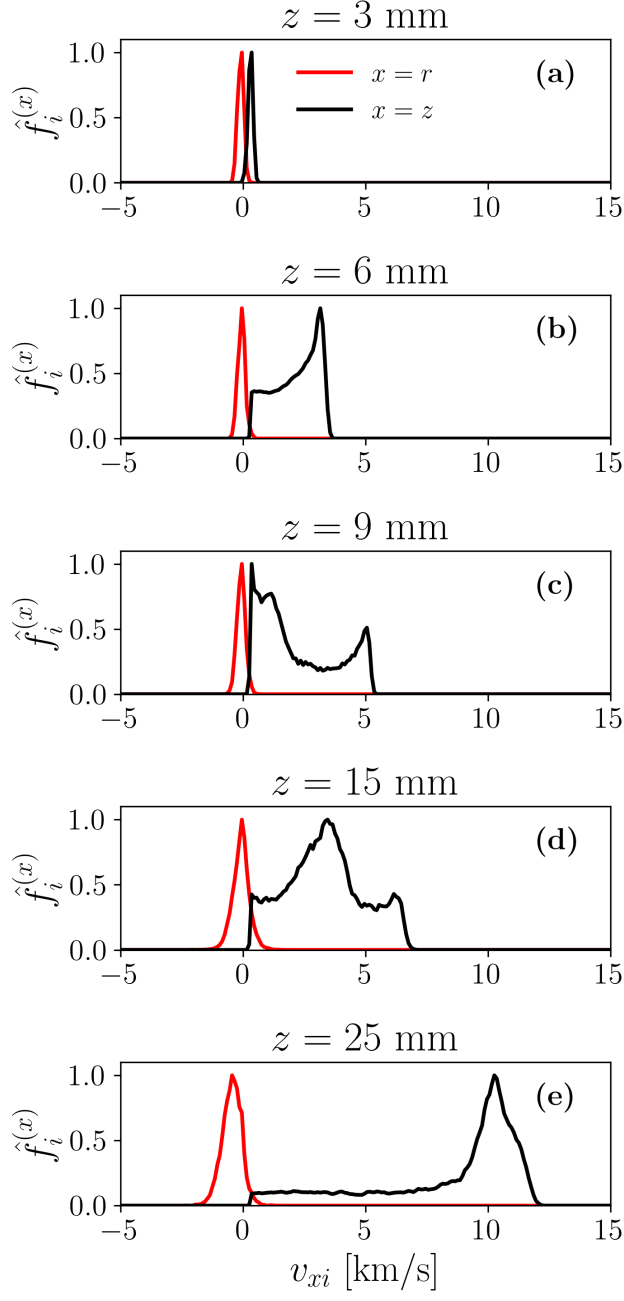


FIG. 10. Ion VDFs at different locations inside the HET channel.

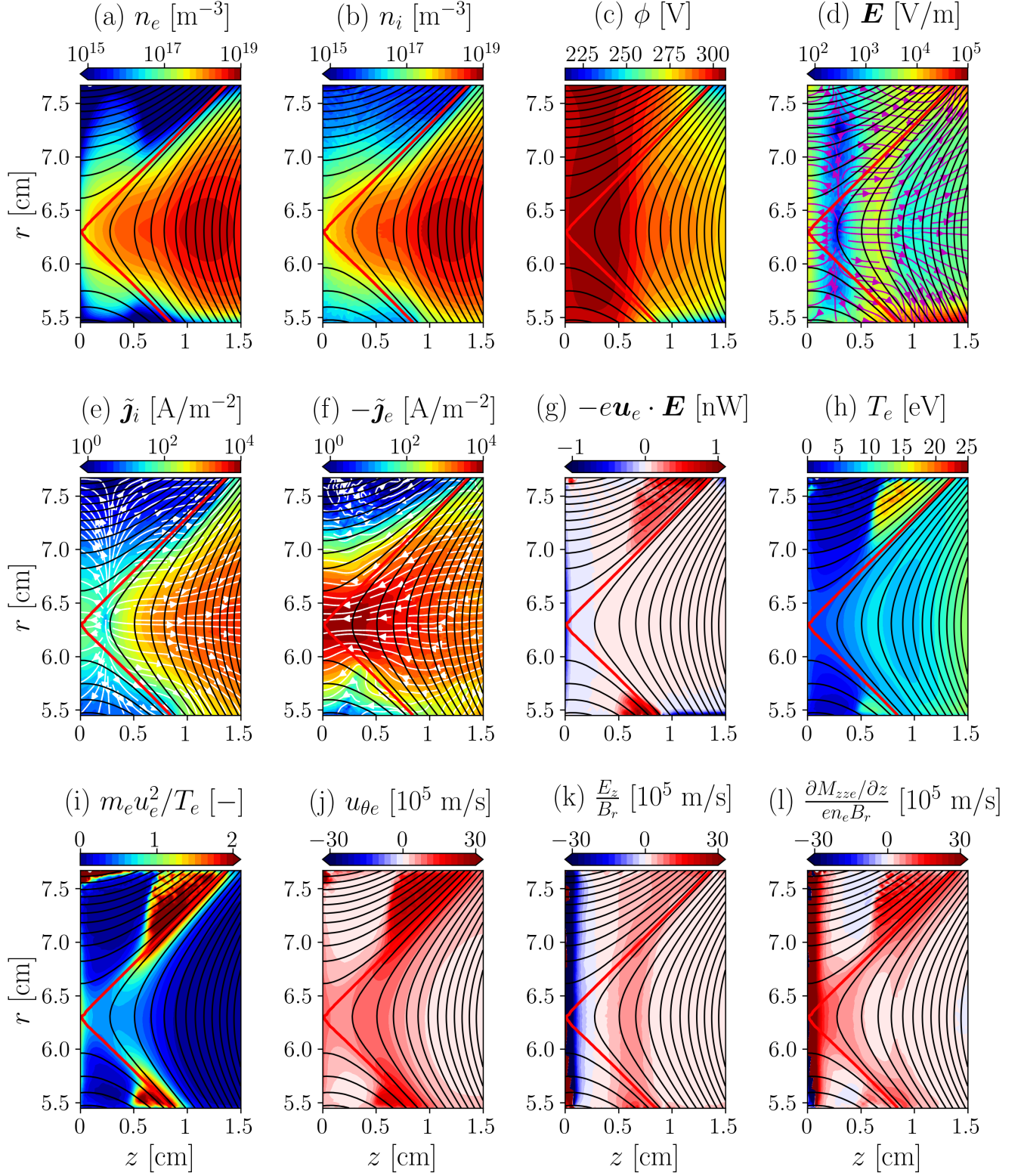


FIG. 11. Macroscopic plasma variables near the anode: (a) electron density, n_e ; (b) ion density, n_i ; (c) electric potential, ϕ ; (d) electric field, \mathbf{E} ; (e) longitudinal ion current density, $\tilde{\mathbf{j}}_i$; (f) longitudinal electron current density, $\tilde{\mathbf{j}}_e$; (g) power of the electric field on the electron population per unit particle, $-e\mathbf{u}_e \cdot \mathbf{E}$; (h) scalar electron temperature, T_e . Black contours represent magnetic field lines and the magnetic separatrix is plotted in red.

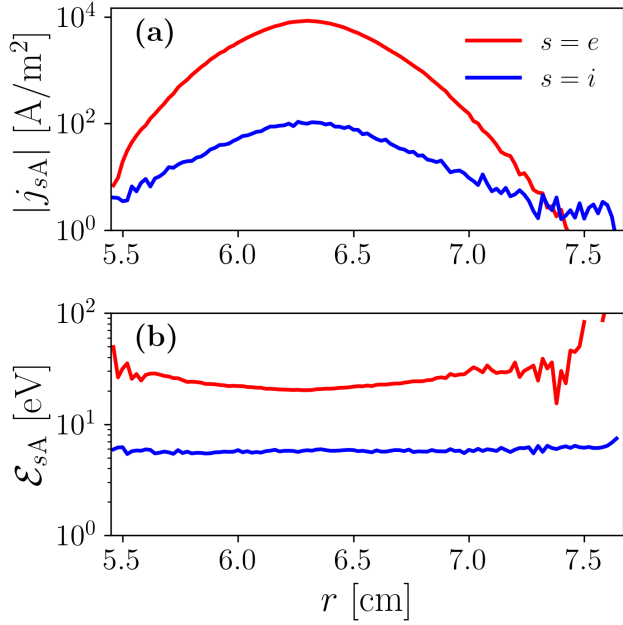


FIG. 12. Wall interaction magnitudes at the anode: (a) current densities, and (b) average impact energies for electrons and ions.

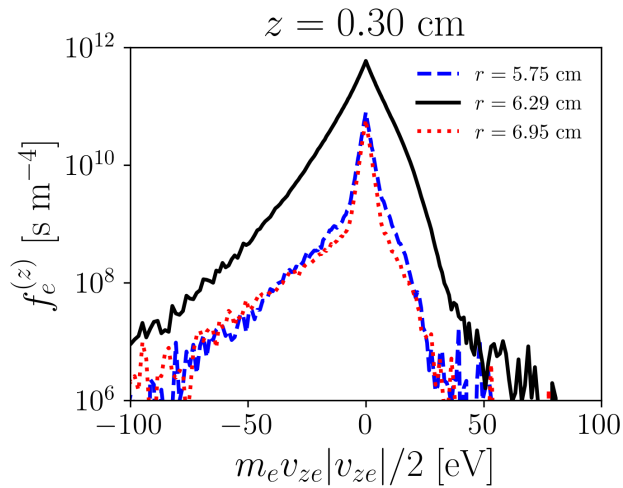


FIG. 13. Electron VDF near the anode wall at different radii.

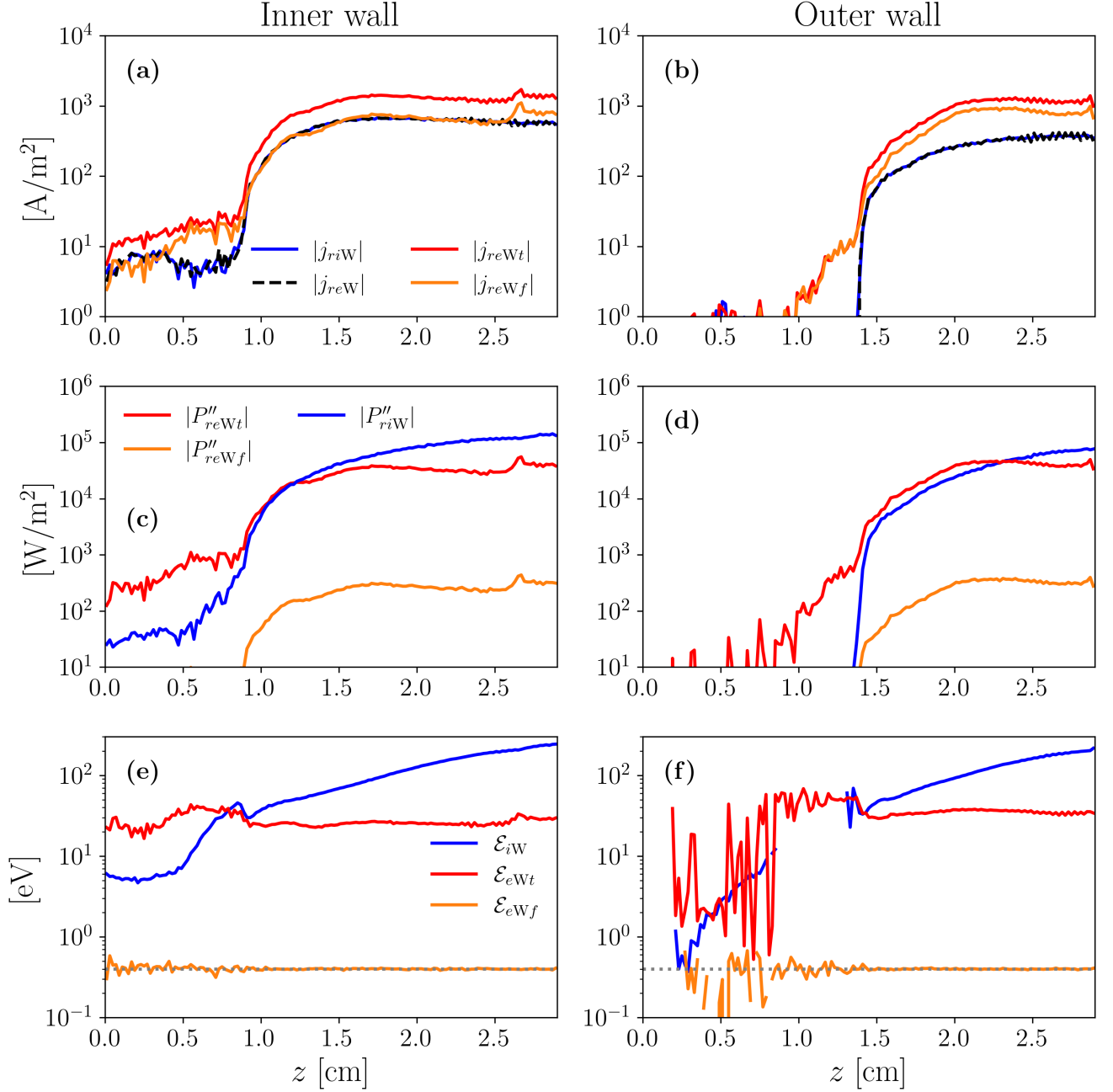


FIG. 14. Wall interaction magnitudes at the inner wall, left column plots, and outer wall, right column plots: (a), (b) ion current density to the wall j_{riW} , electron current density to the wall j_{reWt} , and electron current density from the wall (SEE) j_{reWf} ; (c), (d) ion energy flux to the wall P''_{riW} , electron energy flux to the wall P''_{reWt} , and electron (SEE) energy flux from the wall P''_{reWf} ; and (e), (f) ion energy to the wall \mathcal{E}_{iW} , electron energy to the wall \mathcal{E}_{eWt} , and electron (SEE) energy from the wall \mathcal{E}_{eWf} .

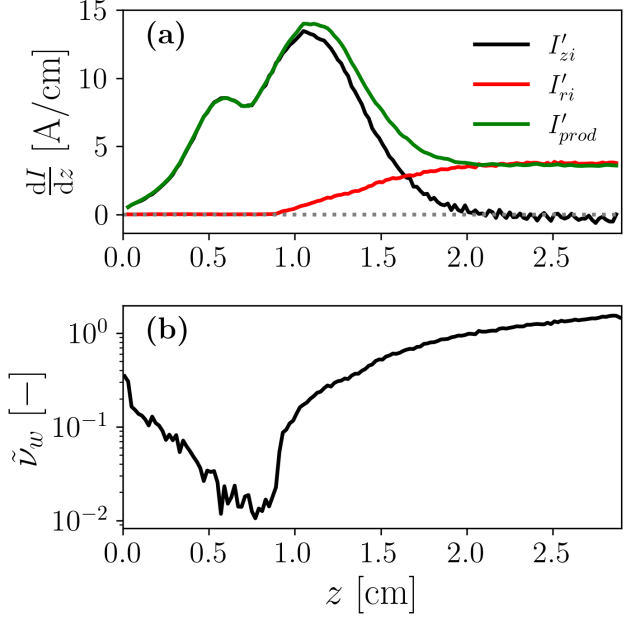


FIG. 15. (a) Current continuity balance showing the contributions of the different terms in Eq. (9) for the ion population. The notation ' $\equiv d/dz$ ' is used in the legend. (b) Non-dimensional wall collisionality parameter defined as in Ref. 24 [Eq. (11)].

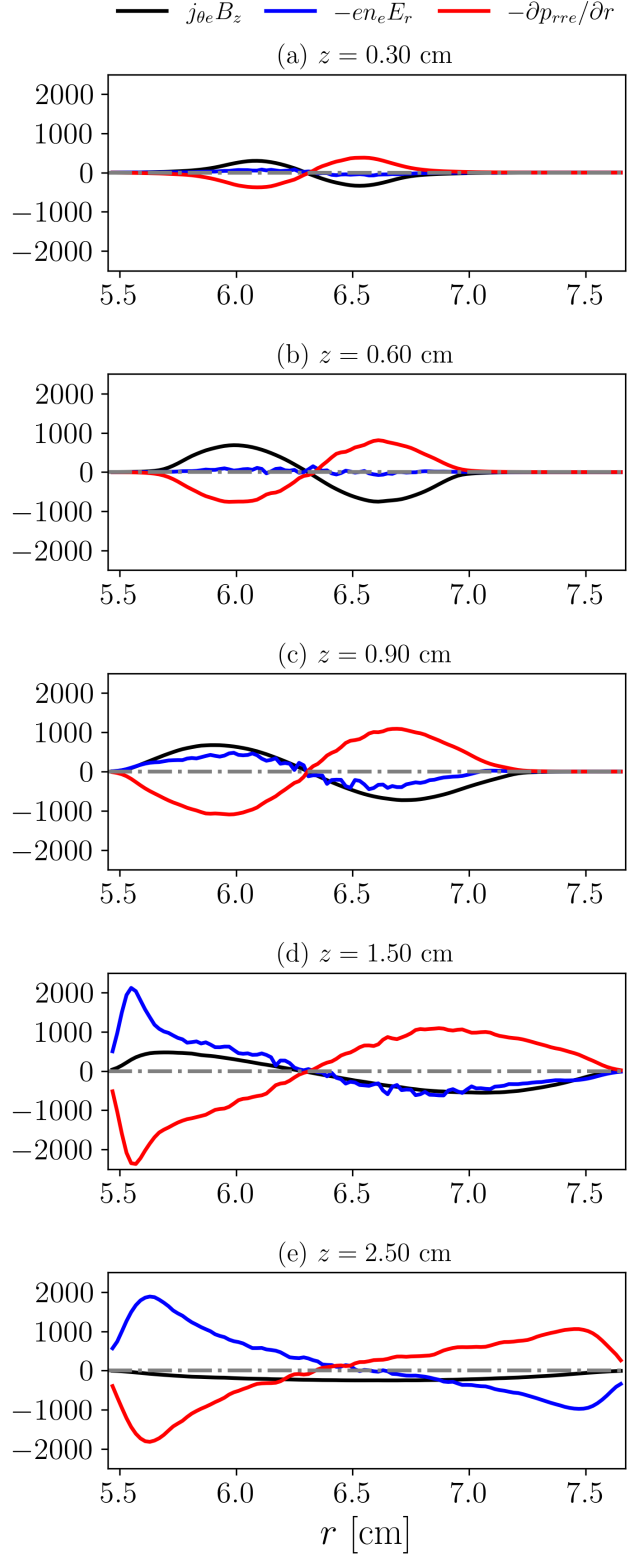


FIG. 16. Main contributions to the radial momentum equation [Eq. (6)] at five different axial sections in N/m^3 .

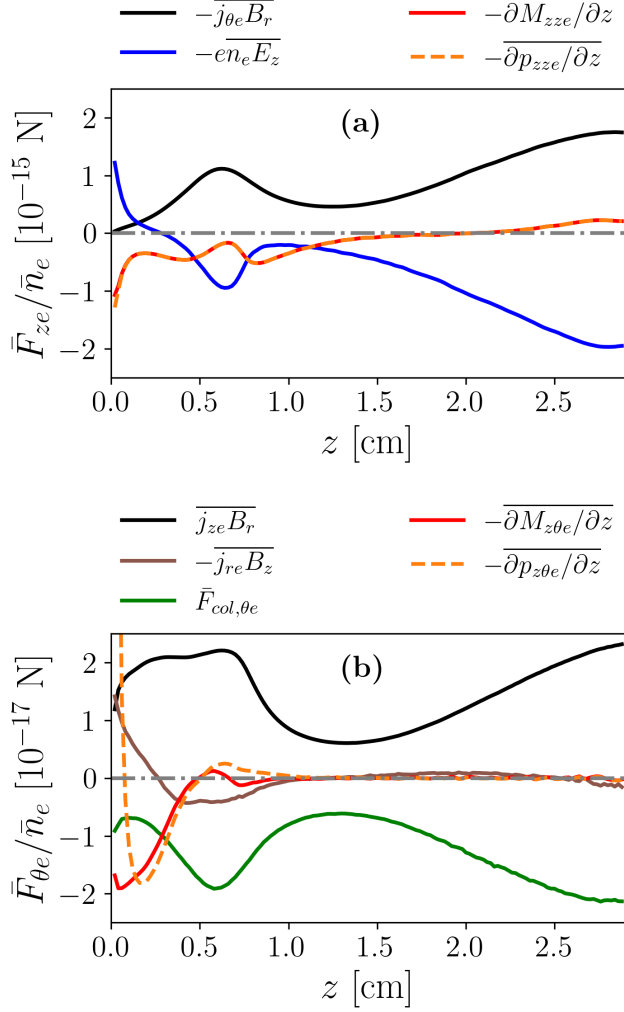


FIG. 17. Radially averaged electron momentum balance. Contributions to (a) the axial electron momentum balance, (b) the azimuthal electron momentum balance.

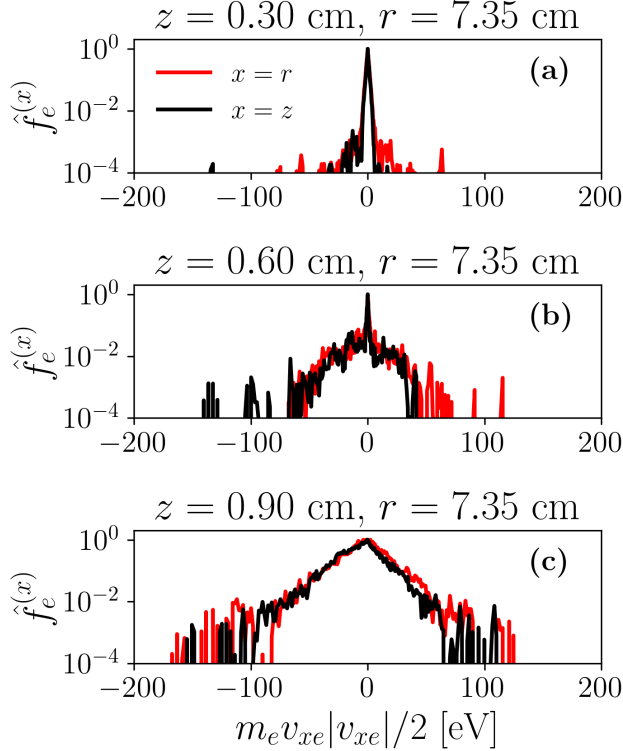


FIG. 18. Electron VDF upstream the magnetic separatrix

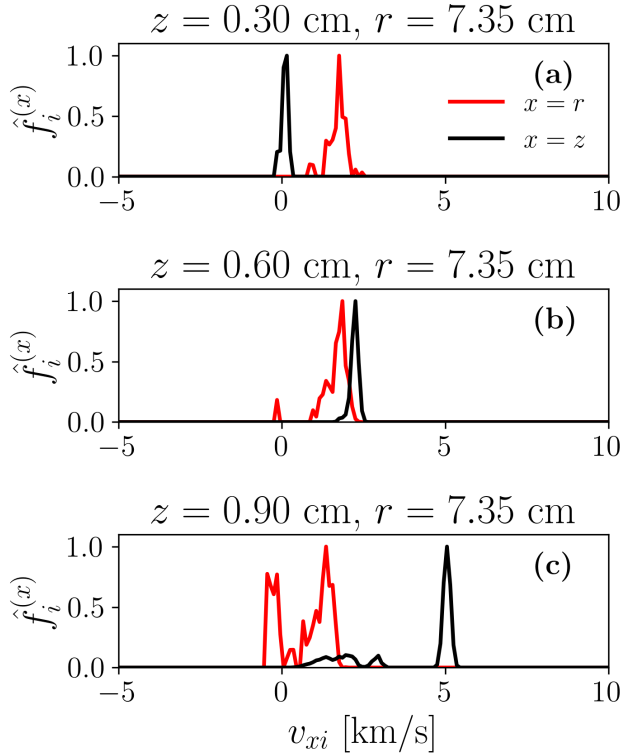


FIG. 19. Ion VDF upstream the magnetic separatrix

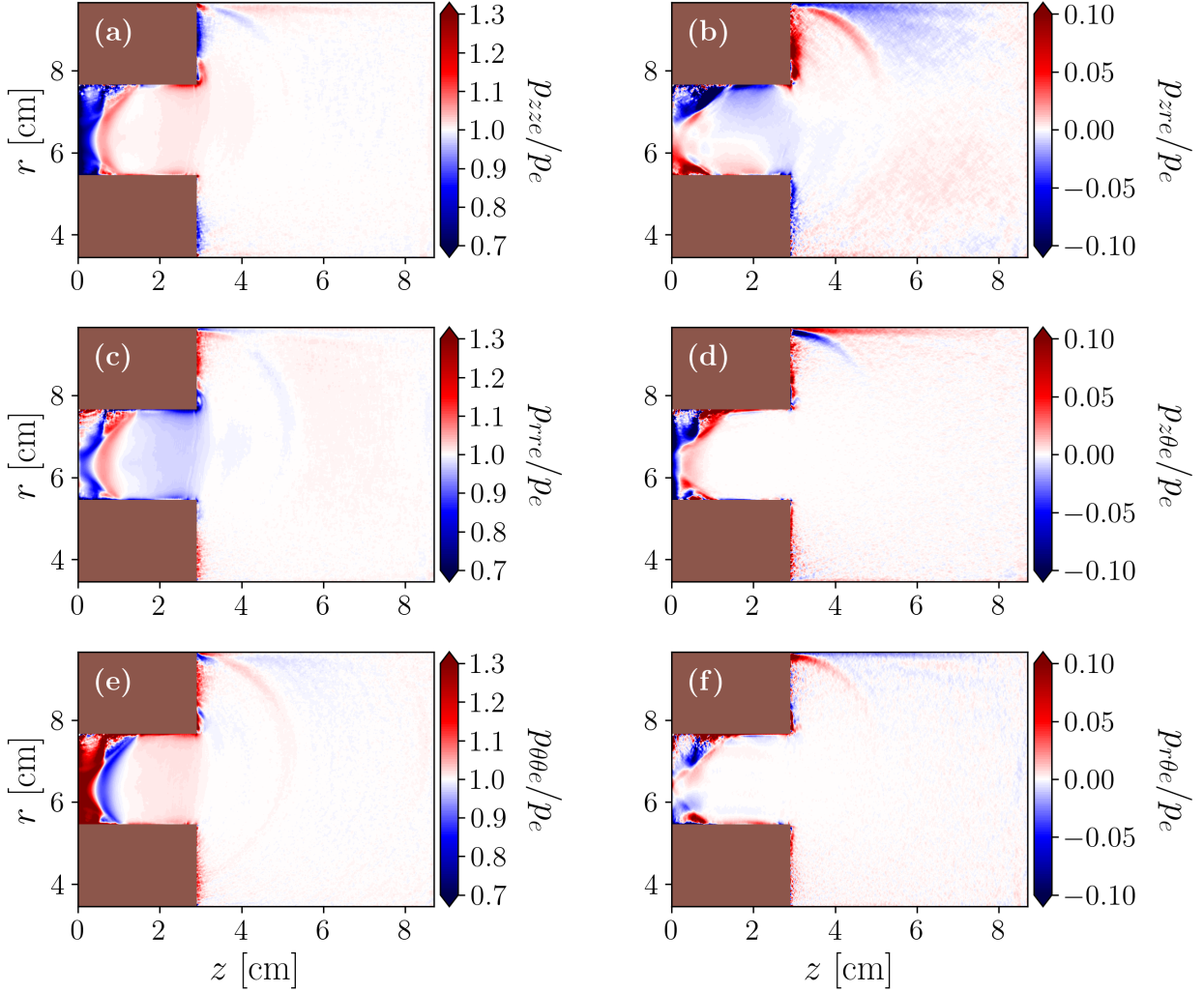


FIG. 20. Pressure tensor components normalized with respect to the scalar pressure $p_e = (p_{zze} + p_{rre} + p_{\theta\theta e})/3$. **AM: guitar y hacer el comentario con las VDFs**

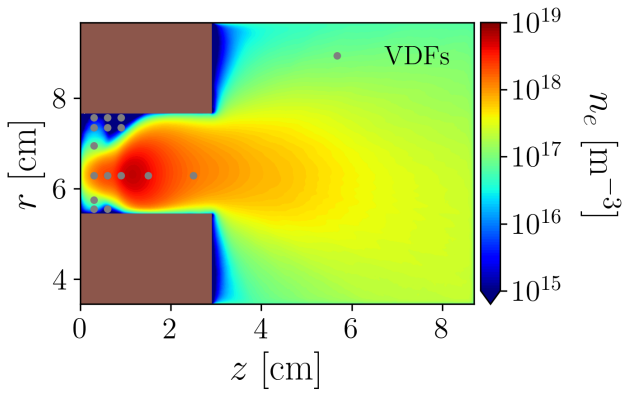


FIG. 21. Locations where the electron and ion VDFs are computed.

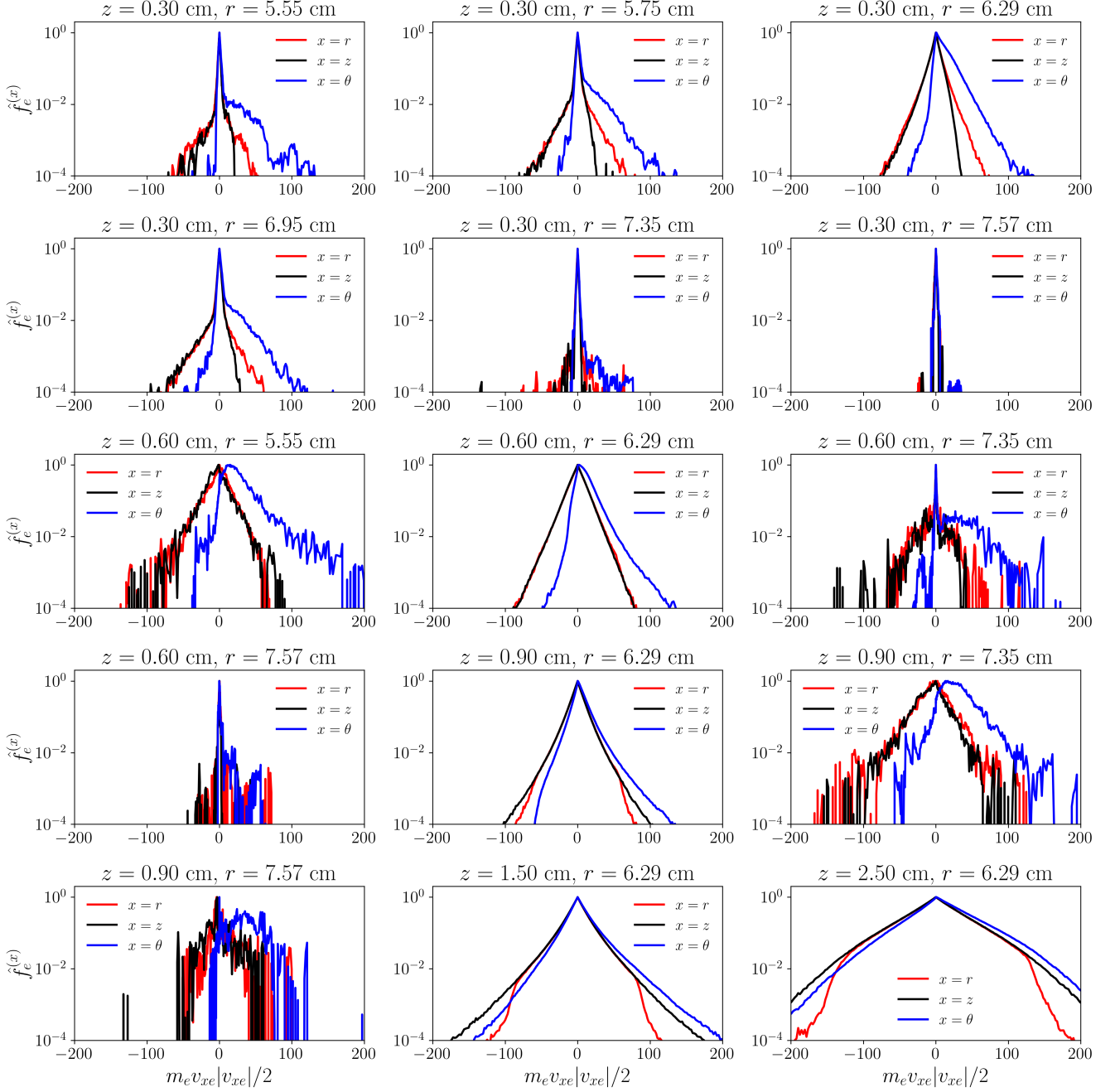


FIG. 22. Electron VDFs at different locations **AM: VDFs en $r = 6.29\text{ cm}$** **AM: Pintar todas las VDFs en $z = 0.3$ en una misma figura**

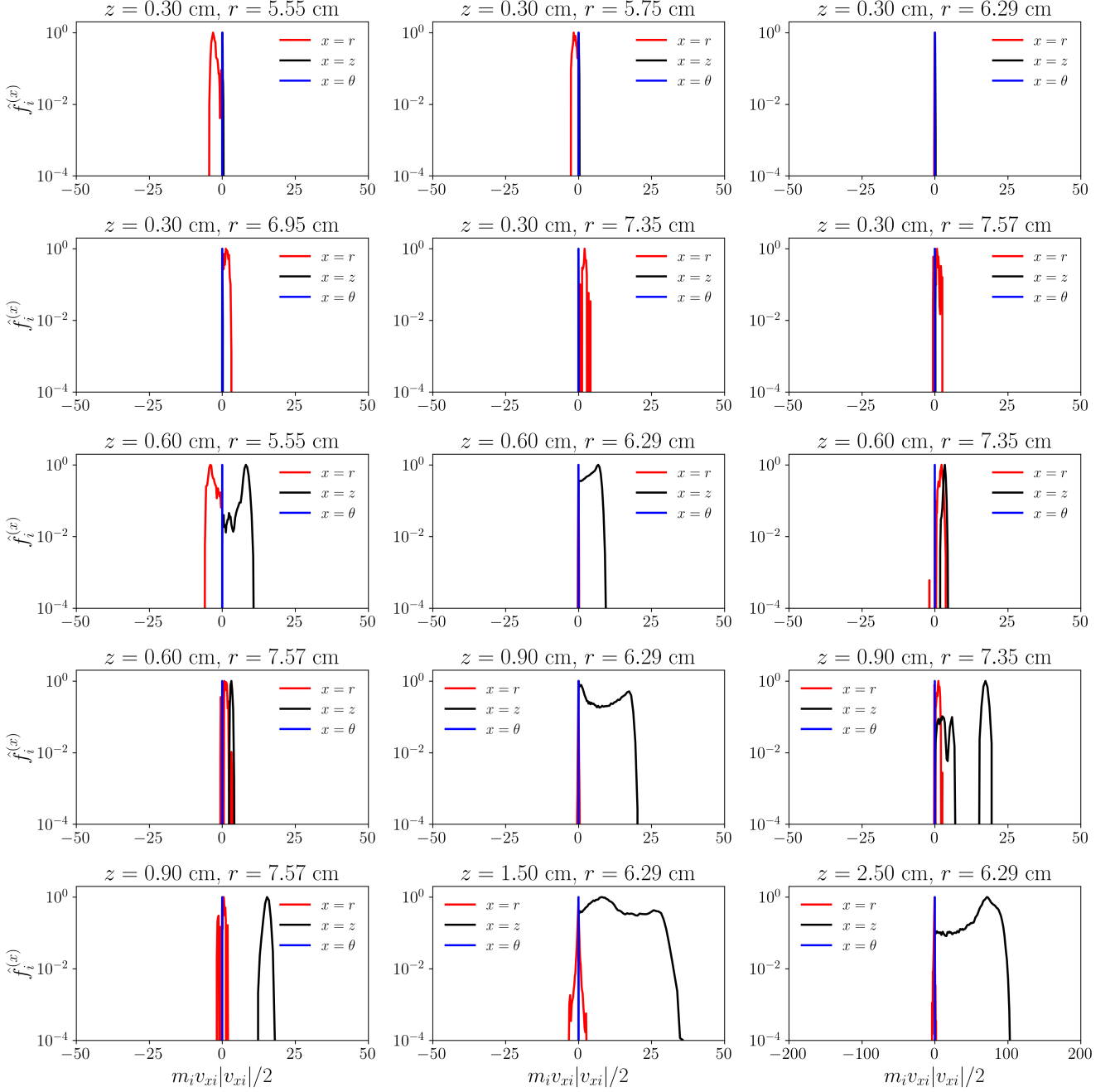


FIG. 23. Ion VDFs at different locations **AM: anisotropia: nos quedamos con la 31, 32, 52**

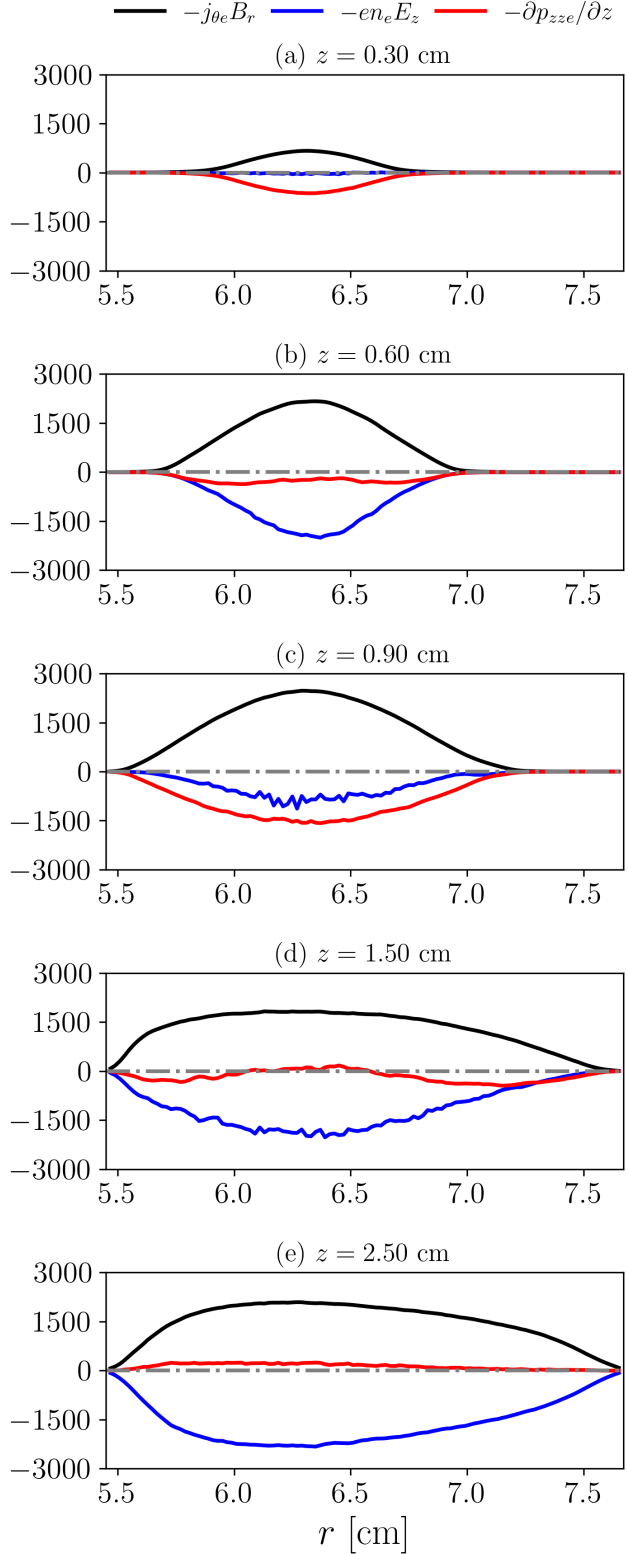


FIG. 24. Main contributions to the axial momentum equation [Eq. (7)] at five different axial sections in N/m^3 . **AM:** Eliminar

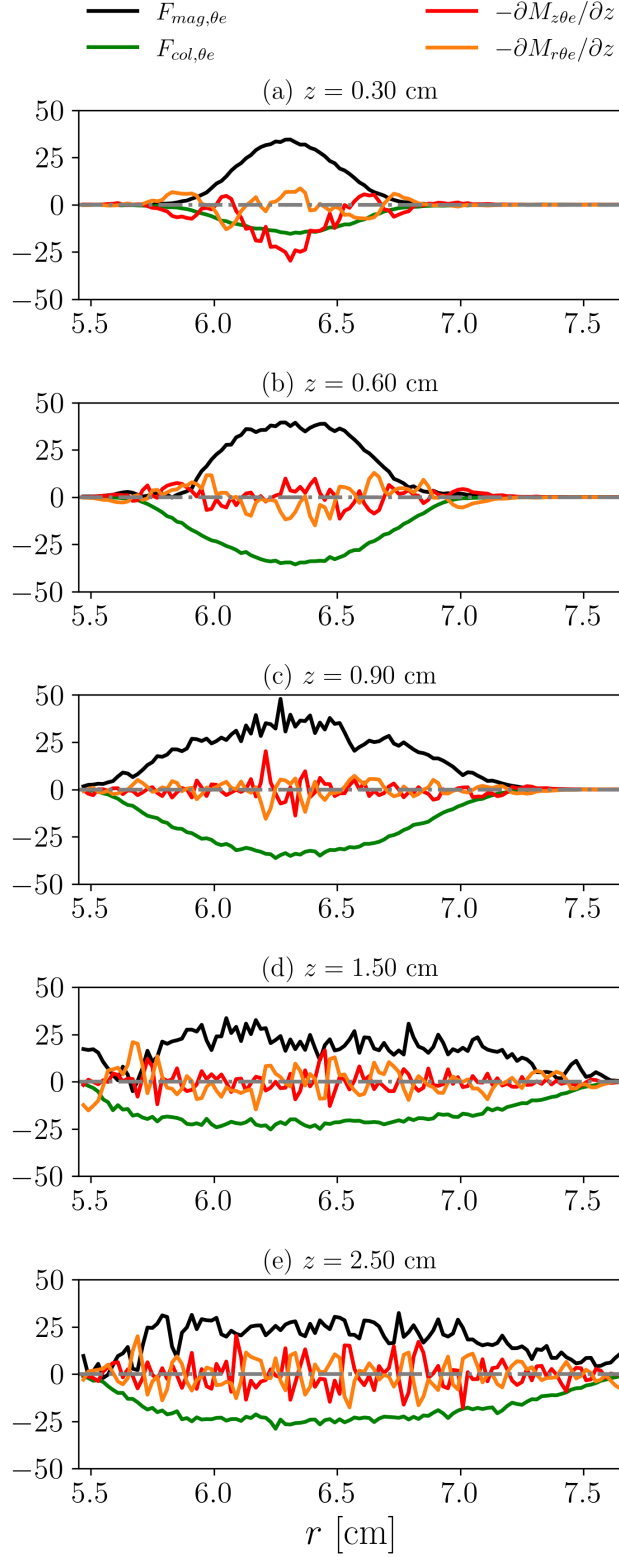


FIG. 25. Main contributions to the axial momentum equation [Eq. (8)] at five different axial sections in N/m^3 . **AM:** Eliminar

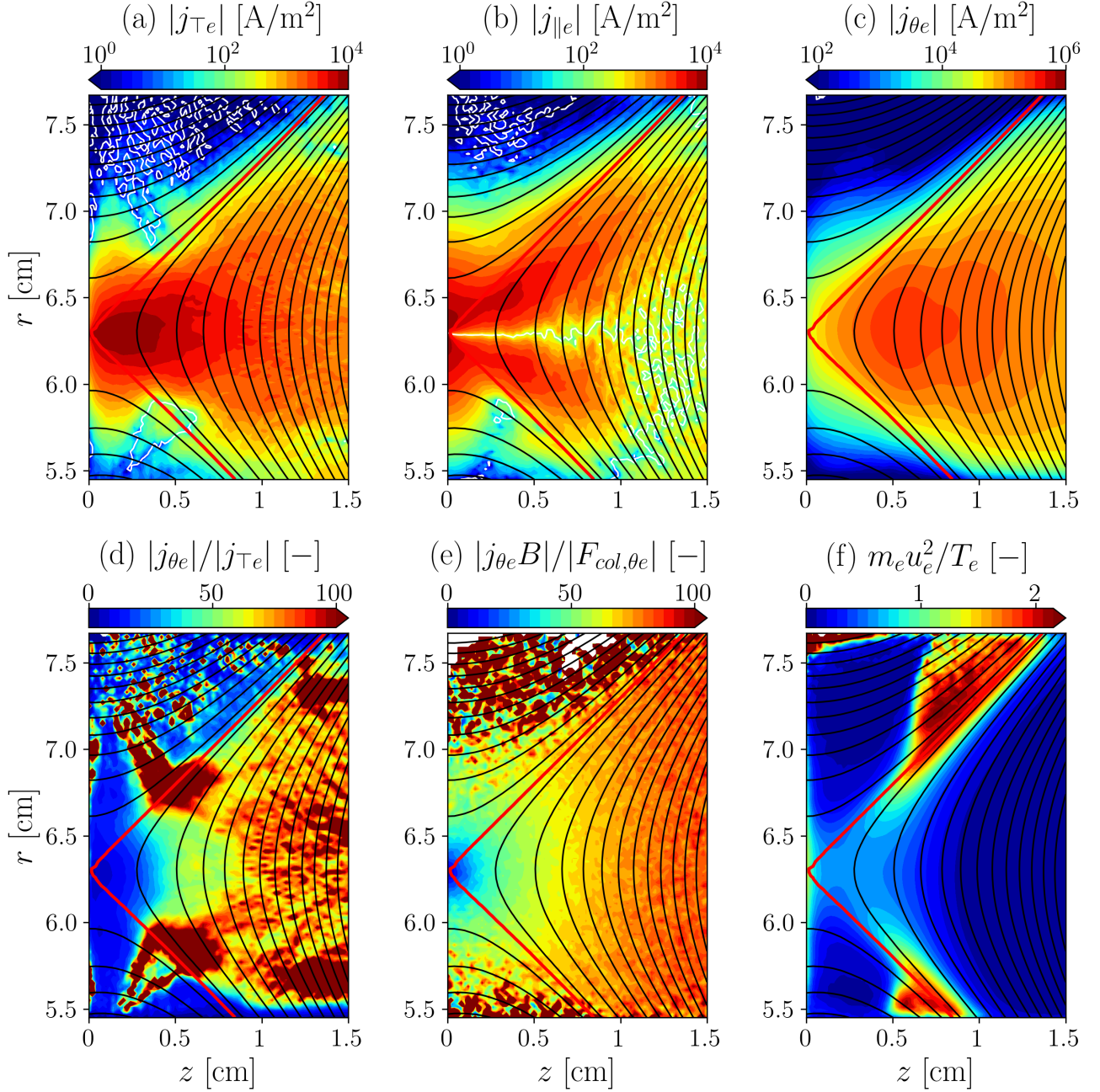


FIG. 26. Other macroscopic plasma variables near the anode: (a) B-perpendicular electron current density, $j_{\perp e}$; (b) B-parallel electron current density, $j_{\parallel e}$; (c) azimuthal electron current density, $j_{\theta e}$; (d) effective Hall parameter, $-j_{\theta e}/j_{\perp e}$; (e) Hall parameter, $j_{\theta e}B/F_{col,\theta e}$; (f) ratio between electron inertia and temperature, $m_e u_e^2/T_e$.

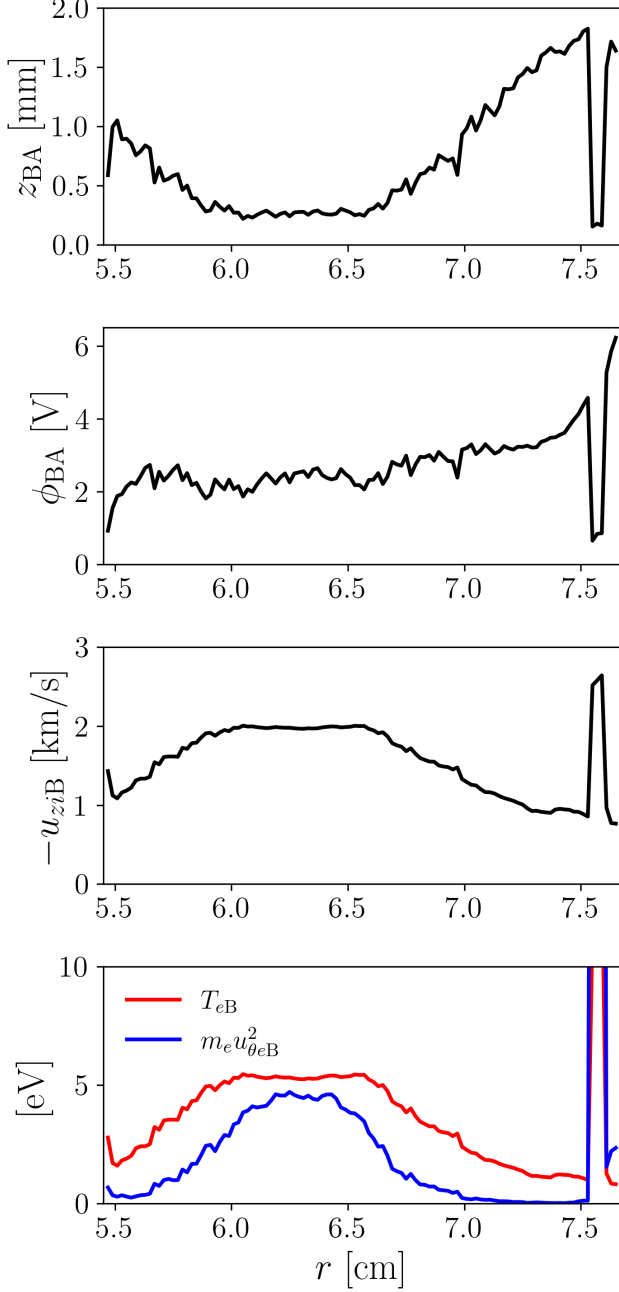


FIG. 27. Anode sheath magnitudes: (a) sheath thickness, z_{BA} ; (b) sheath potential drop, ϕ_{BA} ; (c) axial ion velocity at the sheath edge, $-u_{ziB}$; and (d) electron temperature and azimuthal inertia at the sheath edge, T_{eB} and $m_e u_{\theta eB}^2$ respectively. The sheath edge, B, is considered to be at the location where ions become sonic, $-u_{zi} = \sqrt{T_e/m_i}$.

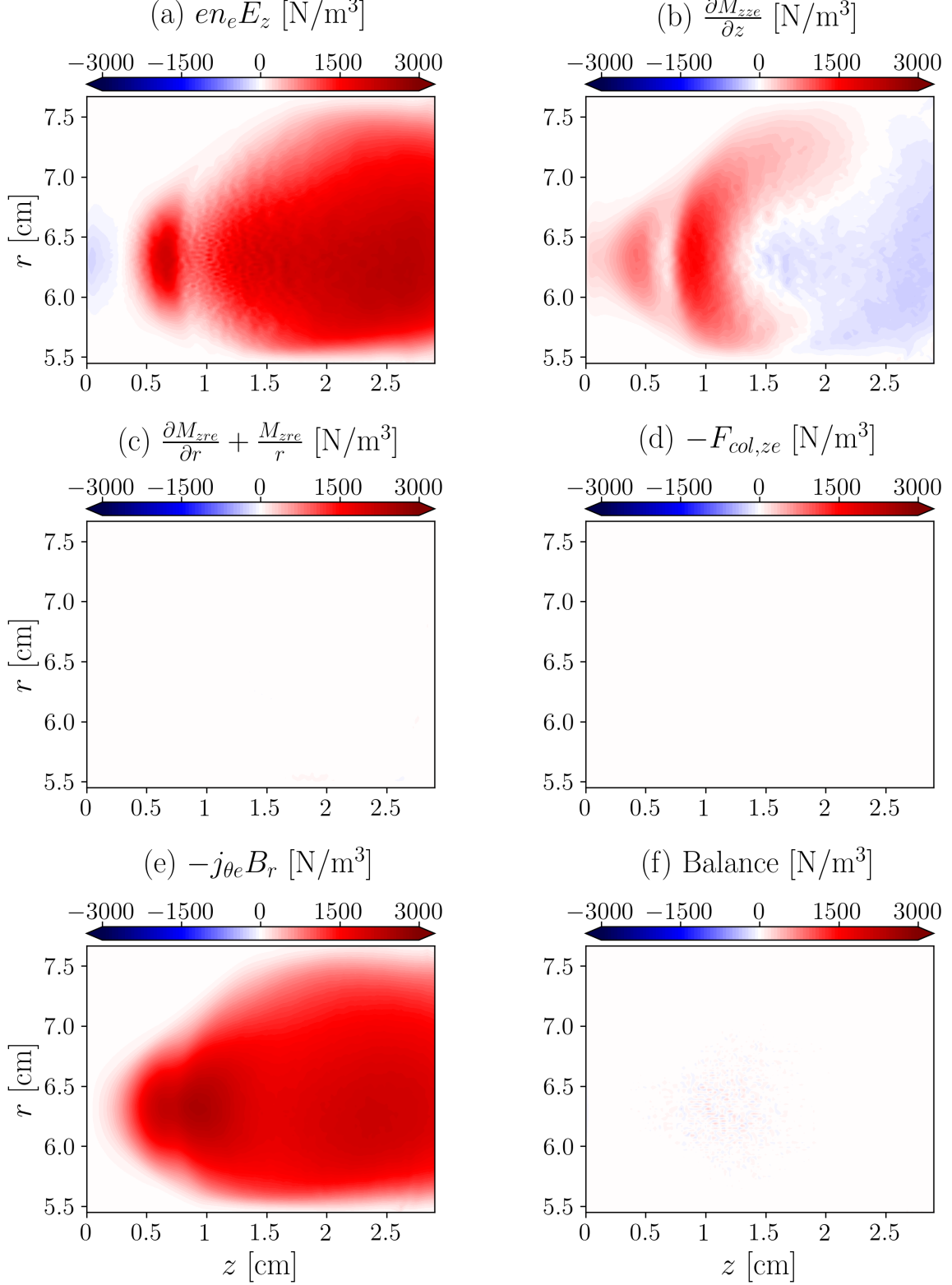


FIG. 28. 2D contributions to axial momentum balance. **AM: Dividir por n_e**